A Framework for Dynamical Seasonal Prediction of Precipitation over the Pacific Islands

H. ANNAMALAI AND J. HAFNER

International Pacific Research Center, University of Hawai'i at Mānoa, Honolulu, Hawaii

A. KUMAR AND H. WANG

Climate Prediction Center, Washington, DC

(Manuscript received 27 June 2013, in final form 18 November 2013)

ABSTRACT

A three-step approach to develop a framework for dynamical seasonal prediction of precipitation over the U.S. Affiliated Pacific Islands (USAPI) is adopted. First, guided by the climatological features of basic variables, a view that climates of the USAPI are connected by large-scale phenomena involving the warm pool, South Pacific convergence zone, tropical monsoons, and subtropical anticyclone is proposed. Second, prediction skill in ensemble hindcasts performed with the Climate Forecast System, version 2 (CFSv2), is evaluated with the hypothesis that ENSO is the leading candidate for large and persisting precipitation departures. Third, moist static energy budget diagnostics are performed to identify physical processes responsible for precipitation anomalies.

At leads of 0–6 months, CFSv2 demonstrates useful skill in predicting Niño-3.4 SST and equatorial Pacific precipitation anomalies. During El Niño, positive precipitation anomalies along the central (eastern) equatorial Pacific are anchored by net radiative flux (F_{rad}) and moist advection (evaporation and F_{rad}). The model's skill in predicting precipitation anomalies over South Pacific (Hawaiian) islands is highest (lowest). Over the west Pacific islands, the skill is low during the rainy season. During El Niño, skill over the USAPI, in particular predicting dryness persistence at long leads is useful. Suppressed precipitation over the Hawaiian and South Pacific (west Pacific) islands are determined by anomalous dry and cold air advection (reduced evaporation and F_{rad}). These processes are local, but are dictated by circulation anomalies forced by ENSO. Model budget estimates are qualitatively consistent with those obtained from reanalysis, boosting confidence for societal benefits. However, observational constraints, as well as budget residuals, pose limitations.

1. Introduction

a. Background

Sustained research over the last three decades has demonstrated that seasonal prediction over the tropics, and to a certain degree over the extratropics, is essentially linked to accurate prediction of tropical sea surface temperature (SST; Kirtman and Pirani 2009). Because of their persistence and ability to create diabatic heating anomalies over a large spatial scale, El Niño–Southern Oscillation (ENSO)-related SST anomalies in the tropical Pacific influence global circulation anomalies (Ropelewski and Halpert 1987; Kumar and Hoerling 1998; Su et al. 2001). Apart from ENSO, SST variations in the tropical Atlantic and Indian Oceans that are either ENSO-induced or internal influence both local (Janicot et al. 1998) and remote regions (Annamalai et al. 2007). In coupled models, therefore, accurate prediction of tropical SST anomalies and their translation into precipitation and diabatic heating anomalies are required for skillful prediction of local and remote climate features. Here, we evaluate seasonal prediction skill of precipitation anomalies over the U.S. Affiliated Pacific Islands (USAPI; Fig. 1) in the hindcasts performed with the National Centers for Environmental Prediction (NCEP) Climate Forecast System, version 2 (CFSv2). We also assess the model's representation of physical processes in affecting regional precipitation anomalies.

Dynamical seasonal prediction is still in its infancy over the USAPI, which is home to over 9 million people. Given the steady population increase leading to enhanced

Corresponding author address: Dr. H. Annamalai, International Pacific Research Center, University of Hawai'i at Mānoa, 1680 East-West Road, Honolulu, HI 96822.
E-mail: hanna@hawaii.edu

DOI: 10.1175/JCLI-D-13-00379.1

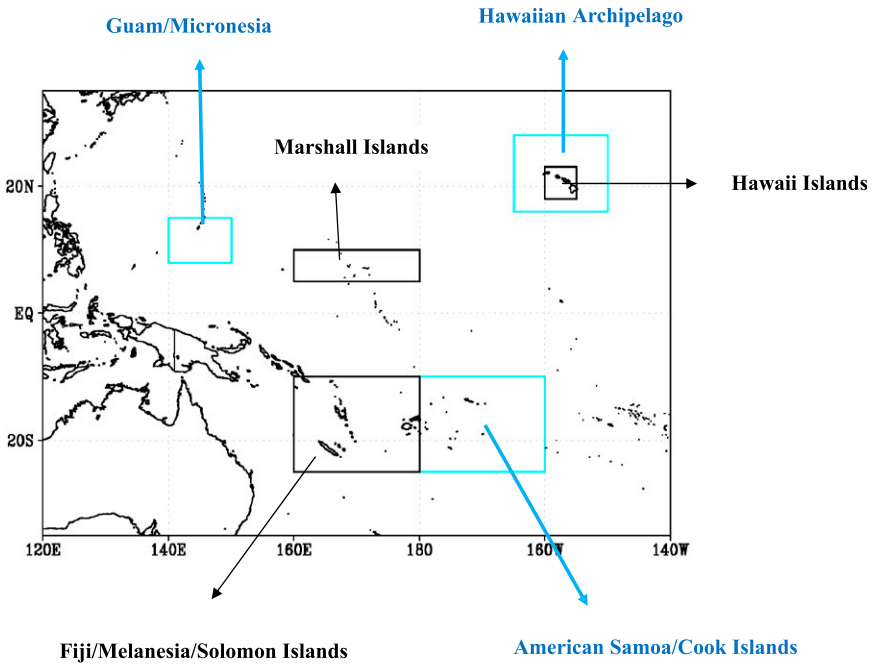

FIG. 1. Map of the Pacific islands. Six regions are considered in the present study: Guam/Micronesia (8°–15°N, 140°–150°E); Marshall Islands (5°–10°N, 160°–180°E); Hawaiian Archipelago (16°–28°N, 165°–150°W); Hawaiian Islands (18°–23°N, 160°–155°W); American Samoa and Cook Islands (25°–10°S, 180°–160°W), and Fiji, Melanesia, and Solomon Islands (25°–10°S, 160°–180°E).

withdrawal of freshwater from the aquifers, and drought conditions affecting both water quality and quantity, skillful prediction of precipitation over the insular USAPI will help planning of freshwater resources. In an earlier study, Sooraj et al. (2012) examined the 15-member ensemble hindcasts performed with the previous version of CFS (CFSv1) from deterministic (anomaly correlation), categorical (Heidke skill score), and probabilistic (rank probability skill score) perspectives. Salient results included the following: (i) high skill was seen in forecasting ENSO-related SST anomalies; (ii) during ENSO, space–time evolution of ocean–atmosphere variables along the equatorial Pacific was realistically represented; and (iii) over the USAPI, forecasting dryness persistence during El Niño was skillful at 3-month leads. Encouraged by the convergence of skill scores, the authors suggested that the development of a dynamical-system-based seasonal prediction for the USAPI is feasible. Yet, a framework or physical basis for such seasonal prediction was not addressed. Recently, Cottrill et al. (2013) found high skill for precipitation anomalies over South Pacific islands in the hindcasts performed with the Predictive Ocean–Atmosphere Model for Australia (POAMA).

In the tropics, seasonal prediction skill is high for large-scale precipitation anomalies, particularly over the open oceans (Shukla 1998), but it remains low for regional-scale anomalies over both open oceans and land. This degradation at regional scales could be as a result of either a lack of physical parameterization schemes to resolve regional processes or large internal variability. If part of the regional-scale precipitation anomalies is determined by large-scale predictable flow patterns, then there is potential for improved skill at predicting regional anomalies. Further, challenges will remain, however, if the internal variability contribution exceeds the part attributable to large-scale flow (Sperber et al. 2000).

b. *Present study*

Here, *framework* refers to a physical basis for our ability to make skillful seasonal predictions. Alternatively, does CFSv2 represent the interactive moist and radiative processes that account for regional precipitation anomalies? If so, confidence in its skill is enhanced for societal benefits.

In pursuit of developing a framework, we adopt a three-step approach:

- Based on the climatological features of precipitation, SST, and atmospheric circulation, we argue that the climates of the individual USAPI regions (Fig. 1) can be interpreted as dynamically connected to large-scale phenomena involving meridional excursions of the

warm pool, South Pacific convergence zone (SPCZ), tropical monsoons, and subtropical anticyclone.

- With the hypothesis that ENSO is the leading candidate for large swings in precipitation over the USAPI, we evaluate seasonal prediction skill in the 24-member ensemble hindcasts performed with CFSv2 for the period 1981–2012. Compared to its previous version (CFSv1), higher horizontal and vertical resolutions and improved physics employed in CFSv2 (Xue et al. 2013) are expected to better resolve processes relevant to ENSO and regional rainfall anomalies. The larger ensemble also provides a better estimate of the signal-to-noise ratio.
- We perform moist static energy (MSE) budget diagnostics, which combines physical processes influencing moisture and temperature, to identify processes that contribute to precipitation anomalies. The interaction between cumulus convection and large-scale circulation is fundamental in the tropics, and such a representation requires consideration of moisture and temperature that is resolved by MSE (Black and Bretherton 2006). We anticipate that the MSE analysis will help identify strengths and weaknesses in model physics, thus informing whether prediction skill is for physically correct reasons.

Brief discussions of CFSv2 hindcasts, MSE budget diagnostics, and observations are given in section 2. The view that climates of individual USAPI regions are dynamically linked is highlighted in section 3. Prediction skills over the equatorial Pacific and specific USAPI regions are presented in section 4. Results from budget diagnostics are discussed in section 5. A summary of the results, including discussion of MSE budget residuals, is given in section 6.

2. Hindcasts, methods, and observations

a. The forecast data

We evaluate the hindcasts performed with CFSv2, based on a fully coupled model (Saha et al. 2014). The atmospheric component is the NCEP Global Forecast System (GFS) at a horizontal resolution of T126 (~100 km) with 64 vertical levels extending from the surface to 0.26 hPa. The oceanic component is the Geophysical Fluid Dynamics Laboratory (GFDL) Modular Ocean Model, version 4 (MOM4), with 40 levels in the vertical, and a zonal resolution of 0.5° and meridional resolution of 0.25° between 10°S and 10°N but gradually increasing through the tropics until fixed at 0.5° poleward of 30° in both hemispheres.

For all calendar months, hindcasts are initialized from January 1982 to December 2012. For each month, predictions with initial conditions (ICs) at 0000, 0600, 1200, and 1800 UTC were made every 5 days starting on 1 January. Here, we use predictions from 24 ICs in each month for subsequent target seasons. For example, for the target month of January, the 24 predictions are from ICs on 2, 7, 12, 17, 22, and 27 December at 0000, 0600, 1200, and 1800 UTC. For model predictions, the ocean and atmosphere ICs are from the NCEP Climate Forecast System Reanalysis (CFSR; Saha et al. 2010; Xue et al. 2011). Here, the zero-month lead (L0) is referred to as prediction initialized from its previous month (e.g., predictions for the month of January are from ICs from December). More details can be found in Saha et al. (2014) and Kumar et al. (2012).

Variables examined include SST, precipitation, and those required to estimate MSE budget [Eq. (2) described below]. Hindcast anomalies are computed by removing model climatology from the ensemble mean for each grid point, each initial month, and each lead time. For MSE analysis, four members that demonstrated high skill in predicting equatorial Pacific precipitation anomalies are chosen.

The ensemble mean is considered as the deterministic forecast from dynamical seasonal prediction methods. Therefore, as a measure of deterministic prediction skill, the anomaly correlation coefficient (ACC) between observed and forecast time series is computed.

Six regions are defined to enclose the USAPI (Fig. 1). For example, over Hawaii the inner box is representative of the main Hawaiian Islands, whereas the outer box encloses all islands in the Hawaiian Archipelago. Over the west Pacific, the box outlined in black (blue) covers the Marshall Islands (Guam, Micronesia, and part of the Northern Marianas). Over the South Pacific, the boxed region in blue (black) represents American Samoa and the Cook Islands (Fiji, Melanesia, and part of the Solomon Islands).

b. Budget diagnostics

The MSE (m) is given by

$$m = C_p T + gz + L_q, \tag{1}$$

where C_p is the specific heat at constant pressure, T is temperature, g is acceleration due to gravity, z is geopotential height, L is latent heat of vaporization at 0°C, and q is specific humidity. The vertically integrated MSE tendency is approximately given by

$$\left\langle \frac{\partial m}{\partial t} \right\rangle' = -\langle \overline{\mathbf{V}} \cdot \nabla m \rangle' - \left\langle \omega \frac{\partial m}{\partial p} \right\rangle' + \mathrm{LH}' + \mathrm{SH}' + \langle \mathrm{LW} \rangle' + \langle \mathrm{SW} \rangle', \tag{2}$$

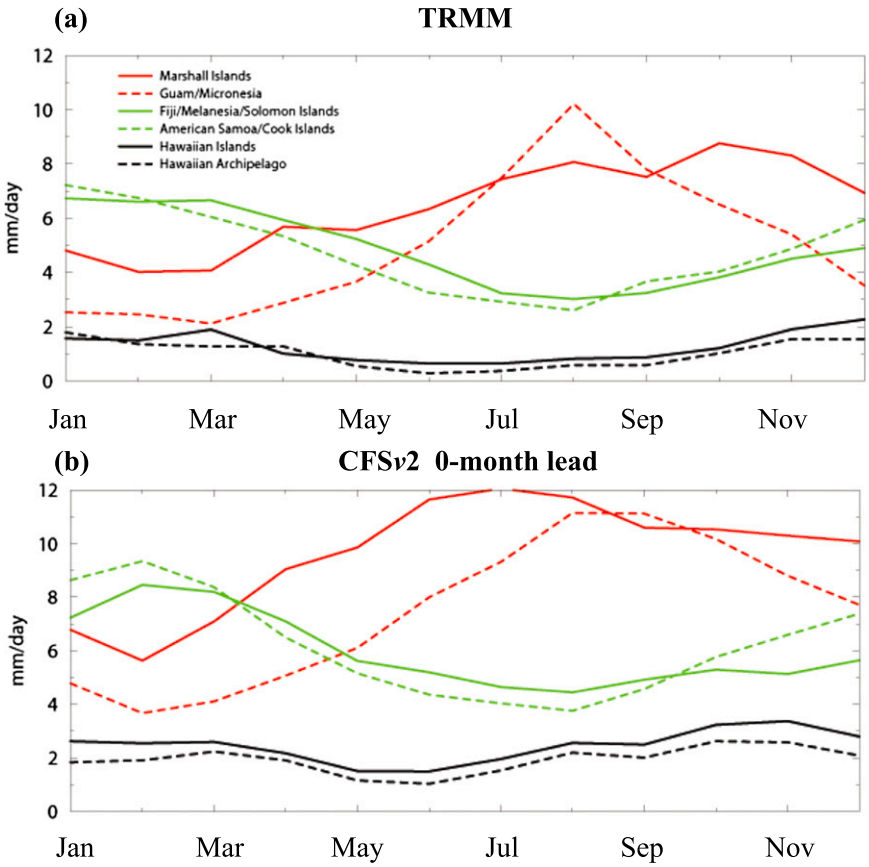

FIG. 2. Temporal evolution of monthly climatological precipitation (mm day^{-1}) averaged over the six Pacific island regions considered in the present study: (a) TRMM-based observations and (b) CFSv2 L0 hindcast.

where $\mathbf{V}'$ is the anomalous horizontal velocity vector, ∇ is the gradient operator, ω' is anomalous vertical pressure velocity, and LH′ and SH′ are anomalous surface fluxes of latent and sensible heat. Terms in angle brackets represent vertical integrals. The terms $\langle \mathrm{LW} \rangle'$ and $\langle \mathrm{SW} \rangle'$ are anomalous net column integrated longwave and shortwave heating rates, and their sum represents net radiative flux F_{rad}. The term $-\langle \omega \partial m/\partial p \rangle'$ represents MSE divergence or its vertical advection. The horizontal advection of MSE $-\langle \overline{\mathbf{V}} \cdot \nabla m \rangle'$ can be split into horizontal advection of moisture $-\langle \overline{\mathbf{V}} \cdot \nabla q \rangle'$ and temperature $-\langle \overline{\mathbf{V}} \cdot \nabla T \rangle'$. Equation (2) combines physical processes influencing moisture and temperature, thereby seeking thermodynamic balance required in tropical phenomena. Under steady-state conditions, an approximation valid at seasonal time scales, the balance in Eq. (2) is between net flux into the column and moist stability, which determines convective processes (Annamalai 2010).

c. *Observations*

For the period 1981–2012, observed datasets used for model verification include the monthly precipitation from the Global Precipitation Climatology Project (GPCP; Huffman et al. 2009), three-dimensional and surface variables from the European Centre for Medium-Range Weather Forecasts (ECMWF) Interim Re-Analysis (ERA-Interim; Berrisford et al. 2009), and the National Oceanic and Atmospheric Administration's (NOAA's) optimally interpolated SST analysis (Reynolds et al. 2002). Additionally, we have used Tropical Rainfall Measuring Mission (TRMM) rainfall observations and TRMM Microwave Imager (TMI) SST (Huffman et al. 2007). The resolution of GPCP is 2.5° × 2.5°, NOAA SST is 1° × 1°, TRMM is 1° × 1°, and ERA-Interim is T255 spherical harmonic representation for the basic dynamical fields and a reduced Gaussian grid spacing (~79 km) for surface fields.

3. Basic states and linkage among USAPI climates

Figure 2a shows observed temporal evolution of precipitation area-averaged over the west Pacific (red), South Pacific (green), and Hawaii (black). Regions covering west and South Pacific islands experience

precipitation year round, peaking during their rainy seasons that coincide with ''local'' summer. The exception is the Marshall Islands (solid red line) that experiences extended summer precipitation. Hawaii, in contrast, experiences wet winters and dry summers, although winter precipitation is less than the dry season precipitation in other regions. In this manuscript, Northern Hemisphere terminology is used for reference to seasons. In the CFSv2 L0 forecast (Fig. 2b), the timing of the wet and dry seasons is well represented, although rainfall tends to be high in all seasons, and also at all leads (Saha et al. 2014). Another exception is that the peak precipitation timing over the west Pacific islands is erroneous.

For the four standard seasons, Fig. 3 (left panels from CFSv2 L0 forecast and right panels from observations) shows the climatology of SST (contours), and precipitation (shaded). Low-level circulation during the corresponding seasons is shown in Fig. 4. In support of the hypothesis that tropical SST determines the location and intensity of near-surface MSE (Neelin and Held 1987), high precipitation occurs over regions of warm SST and low-level convergence (e.g., the SPCZ). CFSv2 forecast climatologies are consistent with this interpretation, and an examination of MSE variations may provide insight into reasons for precipitation anomalies.

The west Pacific islands are located in the warmest surface waters on Earth (Figs. 3a–d). During the extended summer season (June–October), under the influence of low-level moisture-laden westerlies (Fig. 4b), these islands experience the western North Pacific monsoon (WNPM), accounting for peak precipitation (Figs. 2a,b). An examination of observations and models from phase 5 of the Coupled Model Intercomparison Project (CMIP5) suggest that the poleward extension of precipitation is directly associated with a meridional movement of the warm pool (H. Annamalai et al. 2013, unpublished manuscript), which is well captured by the CFSv2 forecast (Fig. 3b). Although not considered here, forecast rainfall is higher along the Himalayan orography.

The climate over the South Pacific islands is influenced by the seasonal migration of the warm pool and the SPCZ (Vincent 1994; Widlansky et al. 2011), leading to a wet season during November through April (local summer) and a dry season from May to October (Figs. 2a,b). The ability of CFSv2 in realistically representing the seasonal cycle of SPCZ is noteworthy. On the large scale, one can conjecture that the north–south movements of the warm pool (SST $>$ 28°C) dictate the precipitation annual cycle associated with the WNPM and SPCZ (Figs. 3 and 4). In this view, seasonal precipitation variations over these islands may be tied to factors that influence meridional migrations of the warm pool, such as ENSO. In addition to Pacific SST changes, ENSO-related SST variations over the tropical Indian Ocean, which affect global circulations, may contribute to precipitation anomalies over these islands (Annamalai et al. 2005, 2007).

Unlike the South Pacific and west Pacific islands, Hawaii is outside the warm pool and is not located in a convergence zone. This is, perhaps, the primary reasons for its low annual-mean precipitation (Figs. 2a,b). South of Hawaii is a narrow tongue of warm SST along the central eastern Pacific (approximately 5°–10°N) and the intertropical convergence zone (ITCZ; Figs. 3e–h). For most of the year, because of the presence of a low-level anticyclone to its north-northeast (Figs. 4a–d), Hawaii is under the influence of a trade wind regime that attains peak amplitude in summer. During winter, cyclonic flow over the North Pacific and the intrusion of low-level westerlies southward of about 25°N are prominent features. Under these circulation changes, extratropical storms that originate along the Kuroshio Extension propagate southward, enhancing winter precipitation over Hawaii.

The existence and intensity of the low-level anticyclone (whose center is denoted by ''H'' in Fig. 4) that influences Hawaiian climate is linked to monsoonal heating. Rodwell and Hoskins (2001) emphasized that heating associated with North American monsoon (Figs. 3b,f) accounts for the eastern flanks of the anticyclone through Rossby wave descent, and the Asian monsoon heating forces the equatorward easterly flow as a Kelvin wave response, while the southerly flow on the western flanks feeds moisture to WNPM. Chen et al. (2001) highlighted the role of Asian monsoon-forced stationary Rossby waves and Seager et al. (2003) further emphasized the importance of local air–sea interactions. Nagamura and Miyasaka (2004) suggested the shallow heating–cooling couplets across the west coasts of the subtropical continent (local air–sea temperature contrast) as an explanation for the anticyclone existence. While our focus is different, the implication is that the climates over Hawaii and west Pacific islands are dynamically linked, and similarly those over the South Pacific and west Pacific islands.

The L0 CFSv2 forecast captures the salient large-scale patterns deemed important for the USAPI climates. Compared to observations, forecast precipitation and low-level circulation are stronger across the tropics, whereas SST is more realistic in the model. It is not clear if precipitation biases are attributable to sensitivity of convection to surface instability rather than free troposphere moisture. Compared to the earlier version of CFS (Sooraj et al. 2012), the bias in intensity and westward extension of the Pacific cold tongue is reduced, and

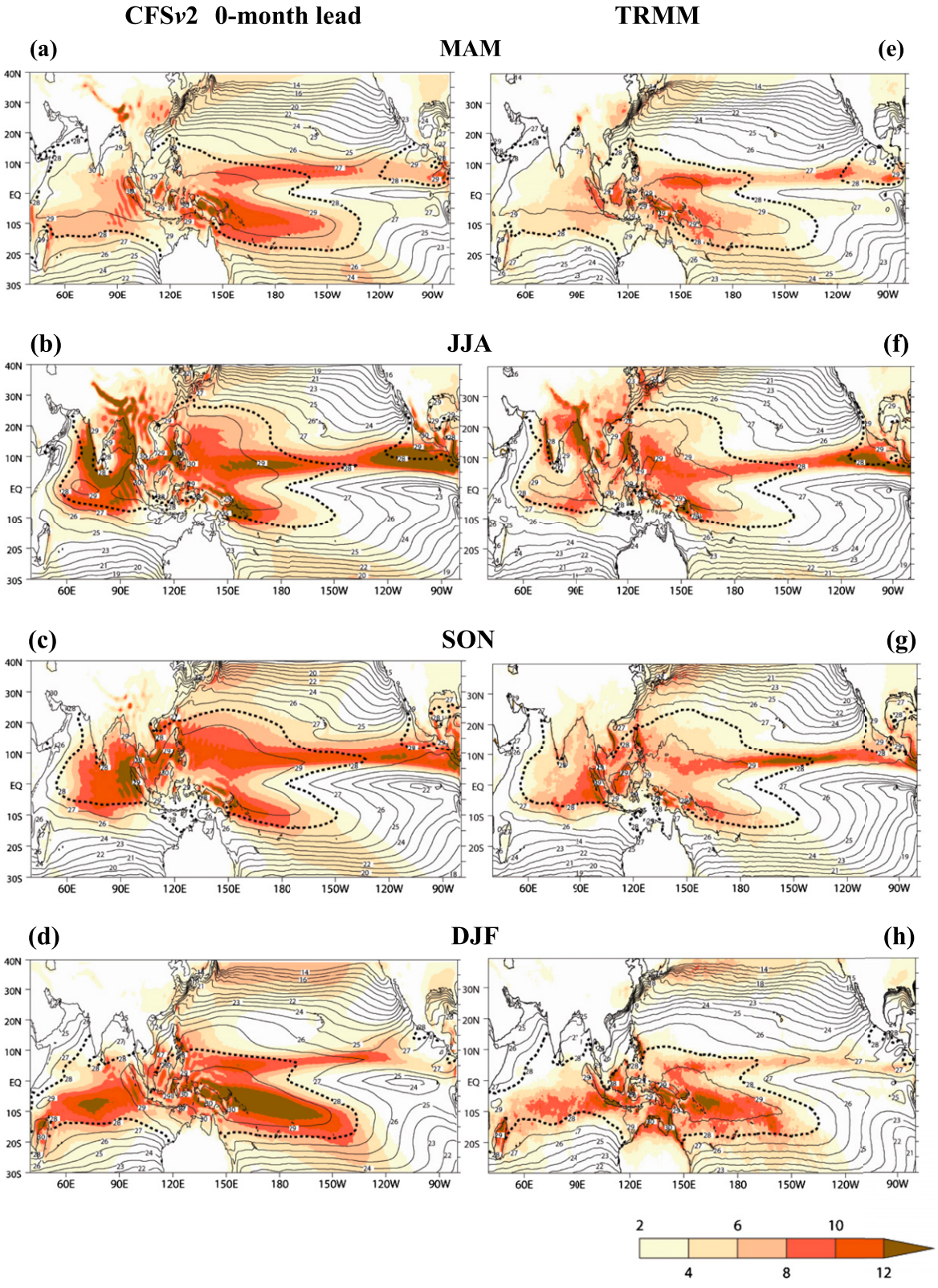

FIG. 3. Climatological seasonal maps of precipitation (mm day^{-1}, shaded) and SST (°C, contour) from (left) CFSv2 L0 hindcast and (right) TRMM-based observations. The 28°C isotherm is shown as thick dotted lines.

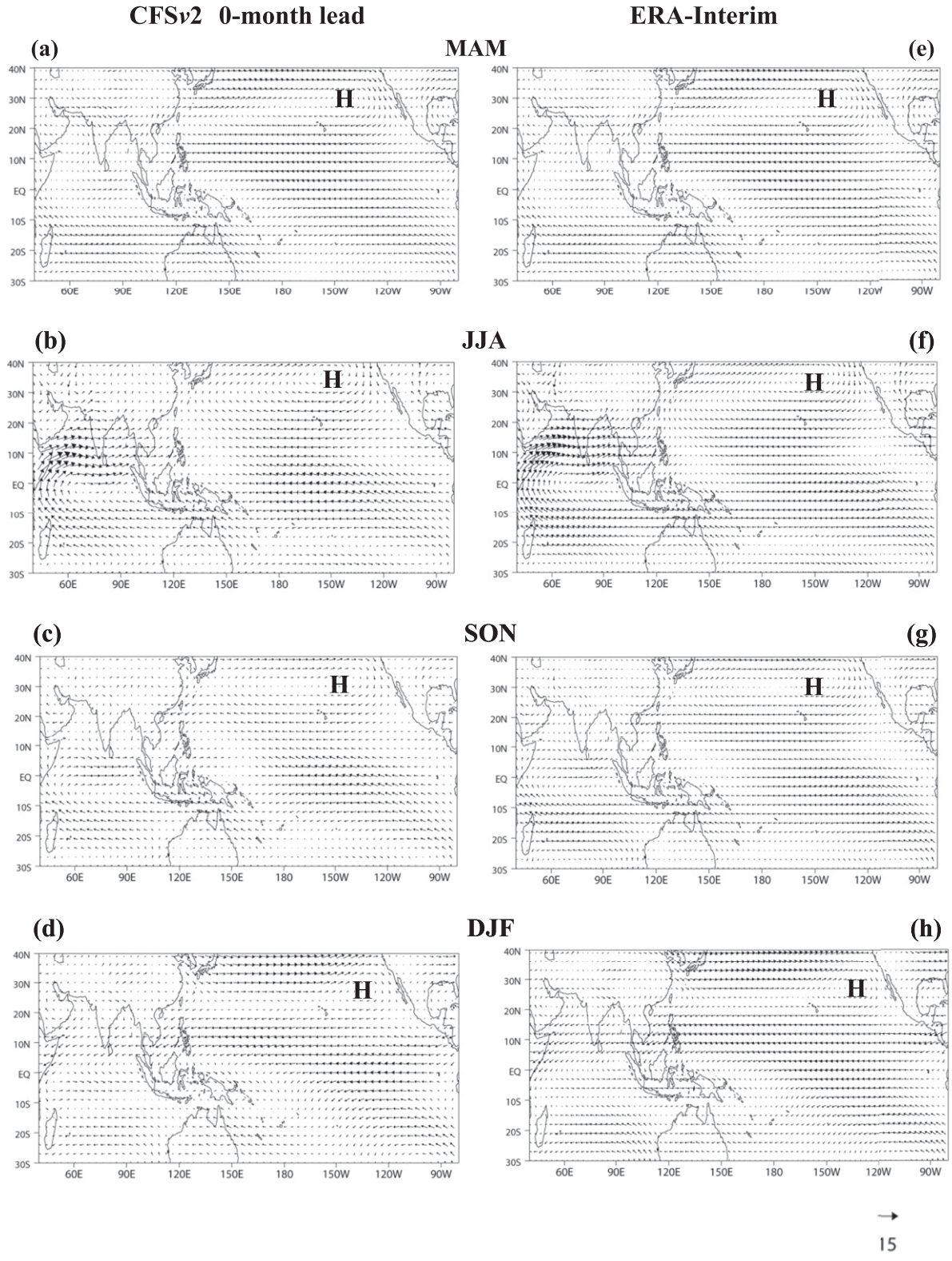

FIG. 4. Climatological seasonal maps of wind ($m\,s^{-1}$) at 850 hPa from (left) CFSv2 L0 hindcast and (right) ERA-Interim; the "H" represents the center of the North Pacific anticyclone. Unit vector is also shown.

poleward extension of the warm pool in the western Pacific is more realistic (Fig. 3b).

4. Hindcast skill evaluation and ENSO-forced teleconnection

For the four standard seasons, Fig. 5 shows variance of seasonal mean precipitation from the forecast (left panels) and observations (right panels). Over both west and South Pacific islands, observations show that during their respective rainy seasons appreciable variability is noted. Over Hawaii, in contrast, both the seasonal mean rainfall (Figs. 2a,b) and its variance are small. These inherent characteristics pose a challenge for successful prediction over Hawaii. Along the equatorial Pacific, precipitation variance with a local maximum around the date line persists throughout the year and peaks in winter, suggestive of ENSO induction. In CFSv2, variance in each of the 24 ensemble members at L0 is estimated individually, and a grand mean is created. In the forecast, while large-scale patterns agree with observations, estimated amplitude is stronger (weaker) over the equatorial central Pacific and along the Pacific ITCZ (Pacific islands).

a. *SST and precipitation prediction along the equatorial Pacific*

For all available forecasts at 0–6-month leads (L0–L6), Fig. 6a shows the skill of hindcasting winter SST anomalies averaged over the Niño-3.4 region (5°S–5°N, 120°–170°W). In almost all strong ENSO events, the L0 forecast closely follows observations but at long leads error is large. This is further supported by high (low) values of ACC for short (long) leads. The model successfully forecasts certain ''double dip'' La Niña events (e.g., 1983–85 and 1998/99) but fails in hindcasting persistent El Niño events (e.g., 1986/87). At long leads, certain false alarms of moderate El Niño events (e.g., 2001) or near-normal conditions (2007/08) are progressively improved as lead time is shortened.

As mentioned in section 1a, the ability of the model's physics in translating the SST anomalies into precipitation anomalies is important for seasonal prediction. For all leads, Fig. 6b shows skill in hindcasting winter precipitation anomalies averaged over the equatorial Pacific (5°S–5°N, 170°E–110°W). The spatially (horizontal and vertical) integrated diabatic heating anomalies over these regions are responsible for forcing global circulation anomalies (Wallace and Gutzler 1981; Su and Neelin 2002). While warm (cold) ENSO events are concurrent with enhanced (suppressed) precipitation, differences in forecast precipitation anomalies between L6 and L0 are about 100%–200%. For instance, during the strongest El Niño event of 1997/98, while predicted Niño-3.4 SST anomalies lie within a range of 0.5°C (Fig. 6a), predicted precipitation anomalies vary from about 4 mm day^{-1} (L6) to about 8 mm day^{-1} (L0). It should also be noted that because model results are based on ensemble mean, the influence of internal variability on seasonal anomalies is suppressed. Further for longer leads, and for a fixed target period, ensemble-mean forecasts also tend to converge to climatological mean with zero anomaly (Peng et al. 2011). The implication is that caution must be exercised in interpreting the model's forecast precipitation amplitude at long leads.

b. *ENSO-forced teleconnection over the USAPI*

Figures 7a–c show results of CFSv2 predicted winter Niño-3.4 SST anomalies regressed onto precipitation anomalies for three selected leads (L0, L3, and L6). At these leads, enhanced rainfall anomalies along the central eastern equatorial Pacific are accompanied with a horseshoe pattern of negative precipitation anomalies covering the SPCZ, tropical west Pacific, and Hawaiian Islands. Barring differences in magnitude, CFSv2 regression patterns are consistent with observations (Figs. 8d,h) except that the narrow tongue of positive rainfall anomalies observed along 0°–5°N, 140°–90°W is forecast at L0.

To appreciate ENSO's influence during its evolution, CFSv2 L0 regression results for other seasons (Figs. 7d–f), and corresponding results from GPCP (Figs. 8a–c) and TRMM (Figs. 8e–g) are presented. In conjunction with results obtained from composite analysis (not shown), the spring pattern (Fig. 7d) is reminiscent of the season following the peak phase of ENSO, whereas the summer (Fig. 7e) and fall (Fig. 7f) correspond to seasons prior to the peak phase of ENSO. Consistent with variance analysis (Fig. 5), model regression coefficients are stronger than either of the observation results. While not explicitly considered here, observed positive precipitation anomalies around French Polynesia (~20°S, 140°W) during winter and the following spring are weakly represented in CFSv2. Regression analysis suggests that, during the warm phase of ENSO, dryness persists for four (two and three) consecutive seasons over the South Pacific (Hawaii and west Pacific) islands. Our results at L0 agree with those estimated from POAMA hindcasts (Cottrill et al. 2013).

During El Niño, the enhanced WNPM during summer may be attributable to low-level cyclonic vorticity arising as a Rossby wave response to enhanced precipitation around the date line (Annamalai and Liu 2005) or as a result of low-level westerly anomalies forced by suppressed precipitation over the eastern equatorial Indian Ocean (Annamalai 2010). The development of dryness in fall and its persistence into the winter and spring is attributed to remote forcing from the equatorial Pacific

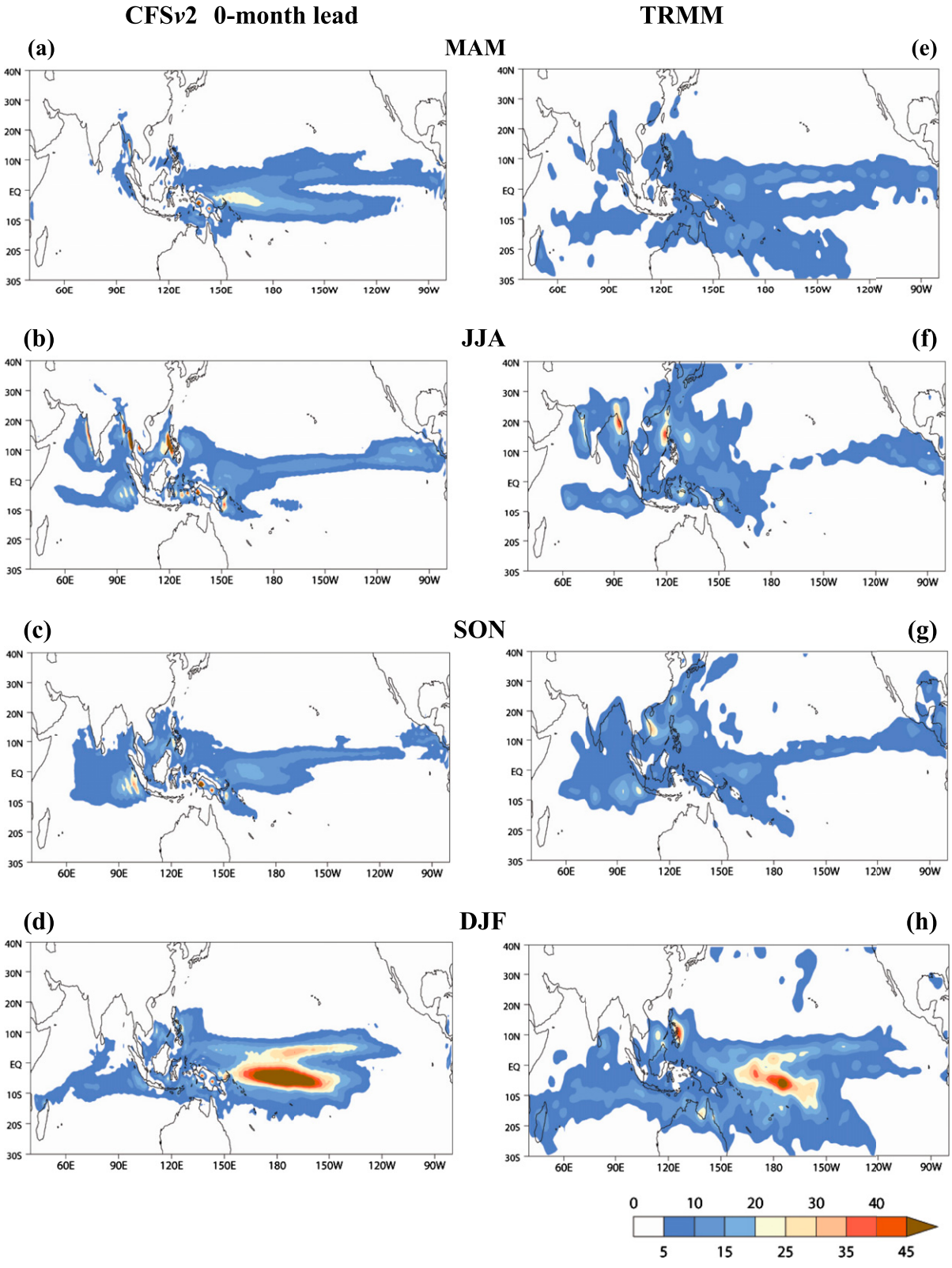

FIG. 5. Seasonal precipitation variance ($mm^2\,day^{-2}$) estimated from (left) CFSv2 L0 hindcast and (right) observations.

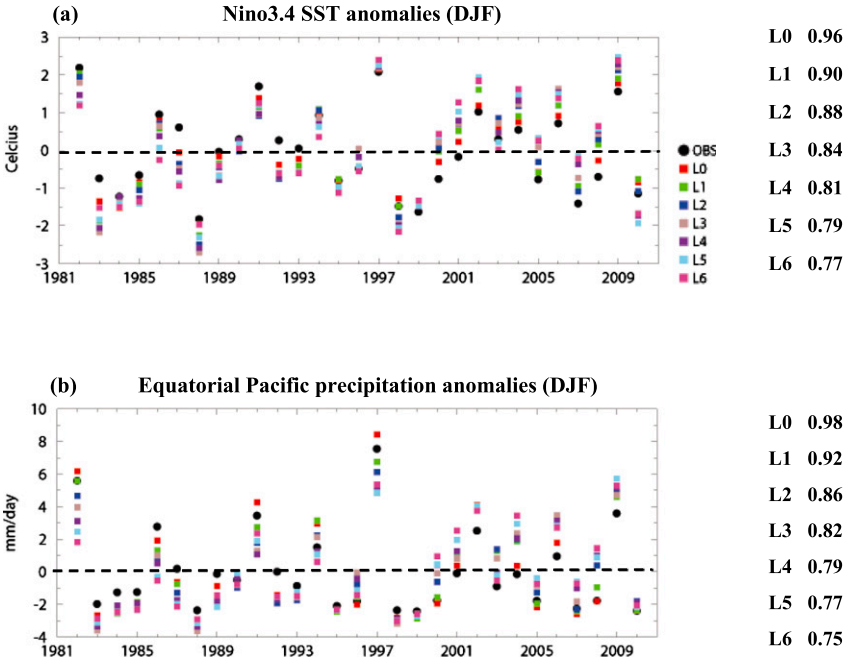

FIG. 6. Temporal evolution of CFSv2 hindcast of winter (DJF) variables at leads 0–6 months: (a) Niño-3.4 (5°S–5°N, 170°–120°W) SST anomalies (°C) and (b) equatorial Pacific rainfall anomalies (mm day^{-1}) averaged over 5°S–5°N, 170°E–110°W. Observations are also shown. The ACC at all leads is provided on the right-hand side.

and local air–sea interactions (Wang et al. 2000). Dryness over the South Pacific is attributable to northeastward migration of the SPCZ (Trenberth 1976; Vincent et al. 2011). Over Hawaii, the descending arm of the local Hadley circulation contributes to dryness. The rising branch of the local Hadley circulation is forced by equatorial Pacific precipitation anomalies. Our interpretation is that ENSO is largely responsible for dryness and its persistence over the USAPI, and therefore skill in predicting its life cycle is important. Compared to its earlier version, prediction of ENSO decay phase improved in CFSv2 (Xue et al. 2013).

c. *Forecast skill over the USAPI*

Figure 9 shows spatial maps of ACC at selected leads. Over regions of high precipitation variance (Fig. 5), ACC exceeds 0.8 at L0 but progressively degrades at longer leads. During winter and the following spring, ACC lies in the range of 0.6–0.8 at L0 over USAPI, but drops to 0.4–0.6 during summer and fall except over the Marshall Islands. At longer leads, lower skill over USAPI is linked to the model's performance along the equatorial central eastern Pacific. Compared to CFSv1 (Sooraj et al. 2012), a marginal improvement is noted in CFSv2.

Figures 10 and 11 show model skill in hindcasting winter precipitation anomalies in individual years. ACC values for all seasons and leads are also provided. Figure 10 (Fig. 11) shows results for boxed regions outlined in black (blue) in Figs. 1 and 9. As in the prediction of Niño-3.4 SST and equatorial Pacific precipitation anomalies (Fig. 6), model skill increases as one approaches L0. In individual winters, apart from predicting large swings during ENSO, CFSv2 hindcasts near-normal conditions correctly in many years; however, some false alarms are evident. In the discussions to follow, ACC $\geq$ 0.6 is considered useful prediction.

Large winter precipitation anomalies over the Hawaiian Islands are tied to ENSO (Figs. 10a, 11a). Given Hawaii's low seasonal mean precipitation (Fig. 2) and associated variance (Fig. 5), predictions from L0 to L2 are useful (Figs. 10d, 11d). Predicting spring precipitation anomalies (e.g., ENSO's decay phase) is useful only at L0. We note that skill over the Hawaiian Archipelago is as good as that over the main islands (Fig. 9).

The Marshall Islands in the west Pacific experience near-normal winter precipitation in about two-thirds of the period analyzed, and except for two of the strongest El Niño events of 1982/83 and 1997/98, ENSO influence is marginal at best (Fig. 10b). A similar view can be expressed for the islands of Guam and Micronesia (Fig. 11b). Here, CFSv2 predictions are useful only at L0–L1 for winter and spring seasons while the skill is too low during the rainy season of July–November (Figs. 10e and 11e), a severe limitation.

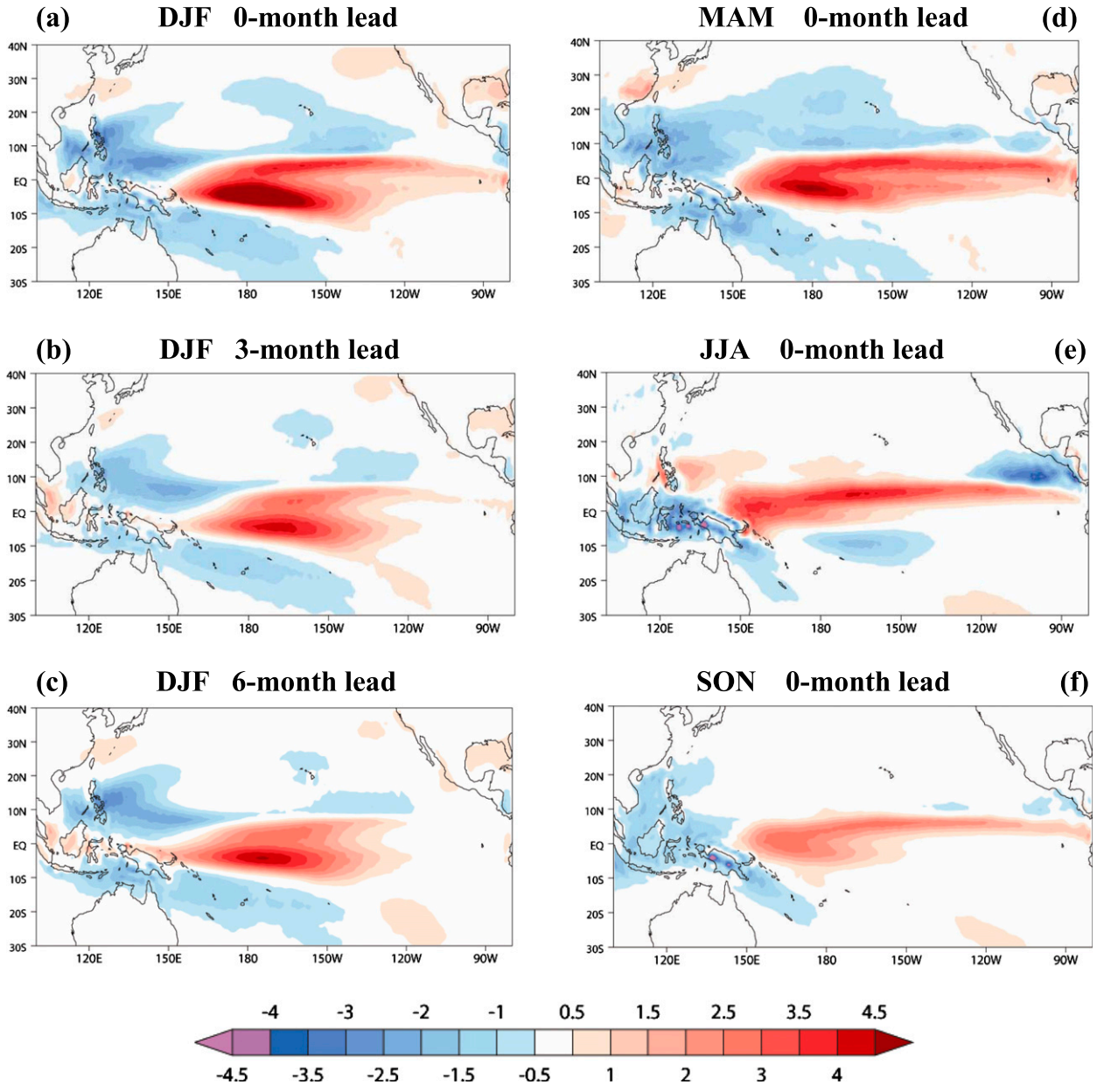

FIG. 7. Niño-3.4 SST anomalies regressed onto precipitation anomalies (mm day^{-1} °C^{-1}) showing results based on CFSv2 hindcast of winter season at leads of (a) 0 (b) 3, and (c) 6 months and CFSv2 hindcast at 0-month lead for (d) March–May (MAM); (e) JJA, and (f) September–November (SON).

During moderate to strong El Niño winters, seasonal precipitation over the islands of Melanesia and Fiji is 30%–50% below climatology (Fig. 10c). While few false alarms are forecast, precipitation variations at these islands demonstrate the highest predictability at all leads and in all seasons, expect during June–August (JJA), the local dry season (Fig. 10f). Our interpretation is that rainfall over this region is under the influence of the SPCZ, which in turn is influenced by ENSO. ENSO's impact on December–February (DJF) precipitation anomalies over the southeastern Pacific islands (the Cook Islands and American Samoa; Fig. 11c) is prominent only during strong El Niño events, consistent with observations (Vincent et al. 2011). However, useful predictions exist for boreal spring (0–3-month leads) and fall (0–6-month leads) seasons (Fig. 11f).

In summary, forecast skill over the Pacific islands is geographically and seasonally dependent. The model-estimated precipitation variance (Fig. 5) is indeed low over the western Pacific and Hawaiian Islands. Whereas

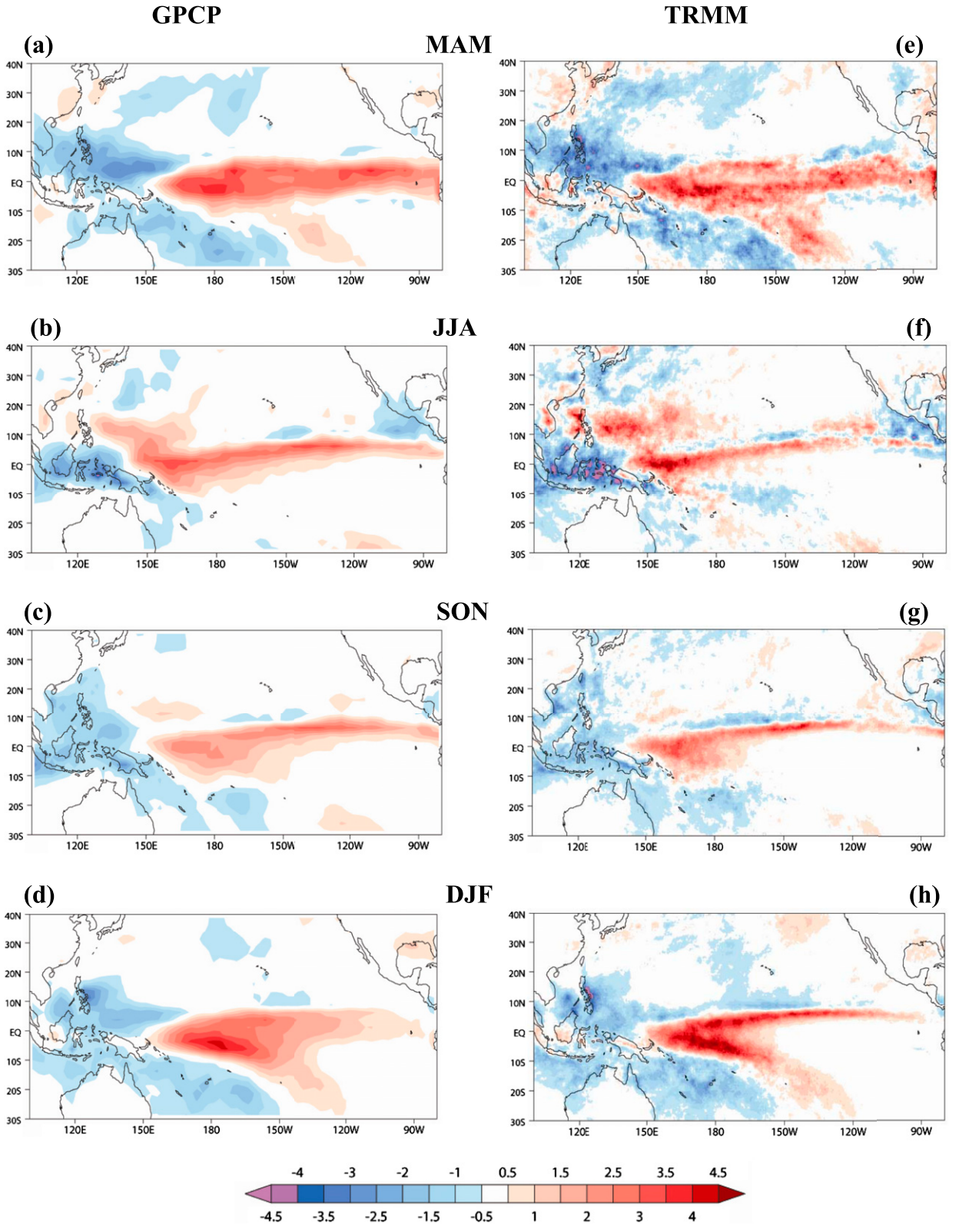

FIG. 8. Niño-3.4 SST anomalies regressed onto precipitation anomalies (mm day^{-1} °C^{-1}) from observations: results based on (left) GPCP and (right) TRMM for (a),(e) MAM, (b),(f) JJA, (c),(g) SON, and (d),(h) DJF.

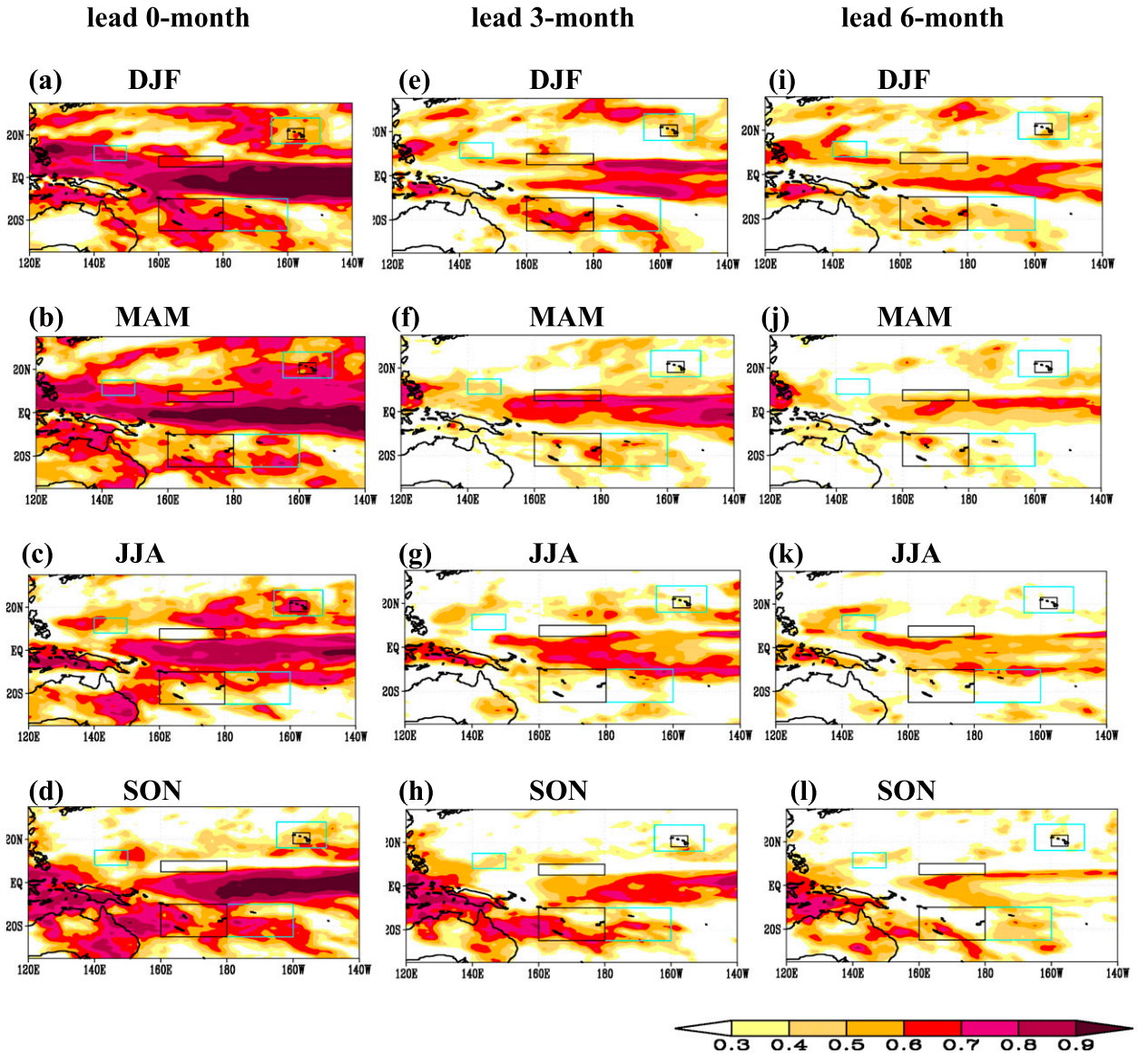

FIG. 9. The ACC between CFSv2 hindcast and observed (GPCP) precipitation anomalies for all seasons and selected leads. Six regions referred to in Fig. 1 are also shown.

regression analysis suggests that the large-scale impact attributable to ENSO is well represented in CFSv2, we speculate that local air–sea interactions and teleconnection from the equatorial Indian Ocean may be underrepresented. Furthermore, over the main Hawaiian Islands, seasonal precipitation is strongly influenced by orography, a factor not adequately represented in CFSv2.

5. Moist static energy budget diagnostics

The convective quasi-equilibrium (QE) hypothesis warrants that temperature and moisture are not independent variables. This constraint allows analysis of anomalous MSE budget to identify possible mechanisms governing tropical precipitation anomalies. In CFSv2, the simplified Arakawa–Schubert convective parameterization scheme that allows the large-scale forcing to make complete use of the convective available potential energy is employed (Caplan et al. 1997), and this scheme underscores the basis of QE constraint (Arakawa and Schubert 1974). However, our recent experience either with reanalysis or model simulations indicates that MSE budget does not close and large residuals exist (Prasanna and Annamalai 2012) but the analysis can still identify leading mechanisms. While we evaluated the budget for

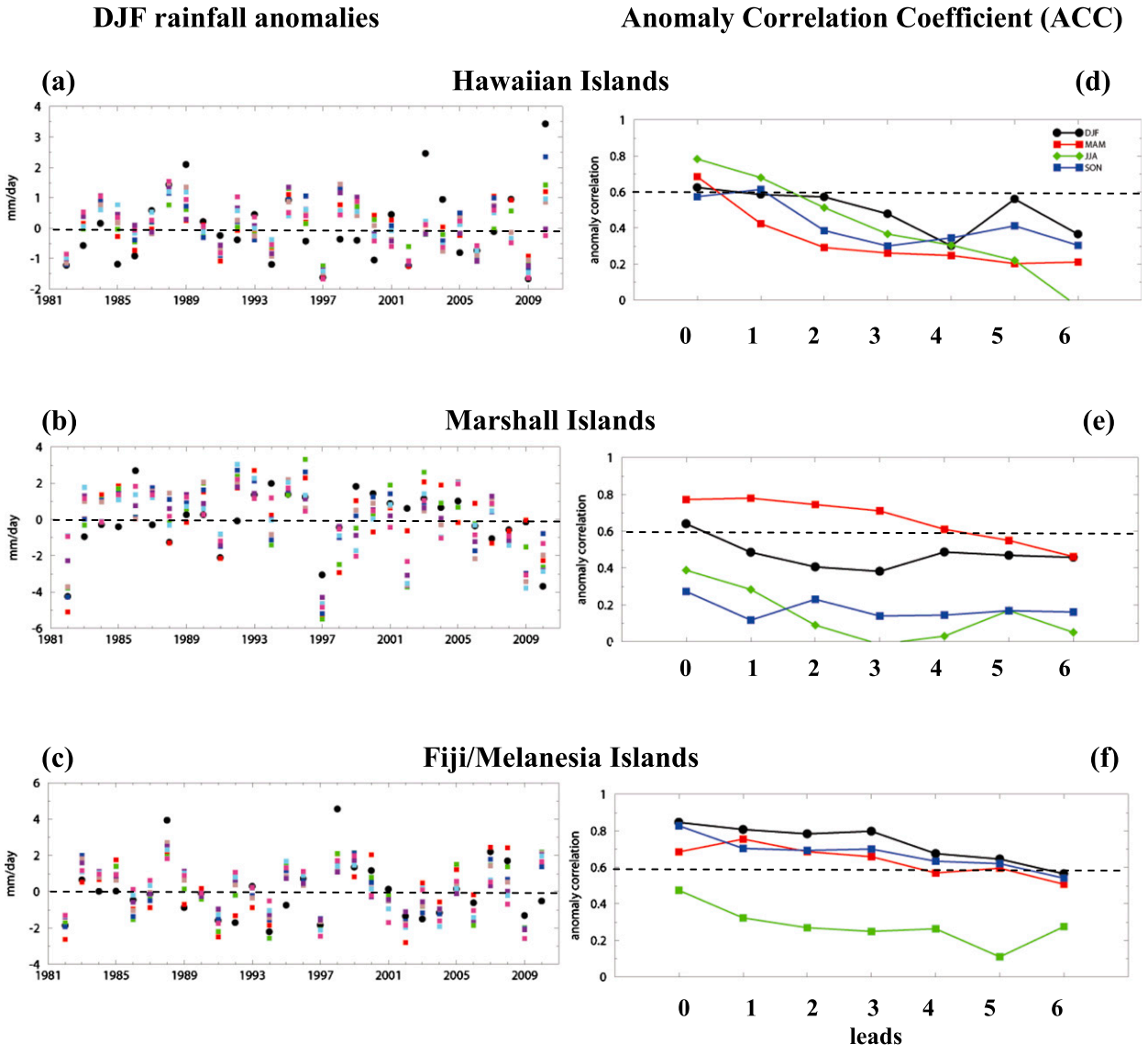

FIG. 10. Temporal evolution of CFSv2 hindcast at leads 0–6 months of winter (DJF) precipitation anomalies over (a) the Hawaiian Islands, (b) the Marshall Islands, and (c) Fiji and Melanesia. The ACC for all seasons and at all leads for (d) the Hawaiian Islands, (e) the Marshall Islands, and (f) Fiji and Melanesia. Dotted line in the right panels corresponds to an ACC value of 0.6. Note that the symbols and colors for (a)–(c) are as in Fig. 6.

individual and composite El Niño and La Niña events, and also for ENSO life cycle, for sake of brevity, we discuss results during the 1997/98 El Niño. We must mention that in the budgets estimated for various classes, deviations in magnitude exist but identified mechanisms remain unchanged.

Figure 12 (Fig. 13) shows budget terms from CFSv2 (reanalysis) for the fall of 1997. Budget results for the winter of 1997/98 are shown in Figs. 14 and 15. We identify $-\langle\overline{\mathbf{V}}\cdot\nabla q\rangle'$ and $-\langle\overline{\mathbf{V}}\cdot\nabla T\rangle'$ as leading terms in certain regions. To get insights, we partition anomalous moisture advection equation into

$$\langle\overline{\mathbf{V}}\cdot\nabla q\rangle' = \langle\mathbf{V}'\cdot\nabla q^c\rangle + \langle\mathbf{V}^c\cdot(\nabla q)'\rangle + \langle\mathbf{V}'\cdot(\nabla q)'\rangle + \overline{\langle\mathbf{V}''\cdot(\nabla q)''\rangle}' . \quad (3)$$

The first term $\langle\mathbf{V}'\cdot\nabla q^c\rangle$ represents the anomalous wind acting on climatological moisture gradient, the second term $\langle\mathbf{V}^c\cdot(\nabla q)'\rangle$ represents climatological wind acting on anomalous moisture gradient, and the third term $\langle\mathbf{V}'\cdot(\nabla q)'\rangle$ represents anomalous wind acting on anomalous moisture gradient. The last term represents contribution from eddies. In Eq. (3), replacing q by T yields various terms of the temperature advection equation.

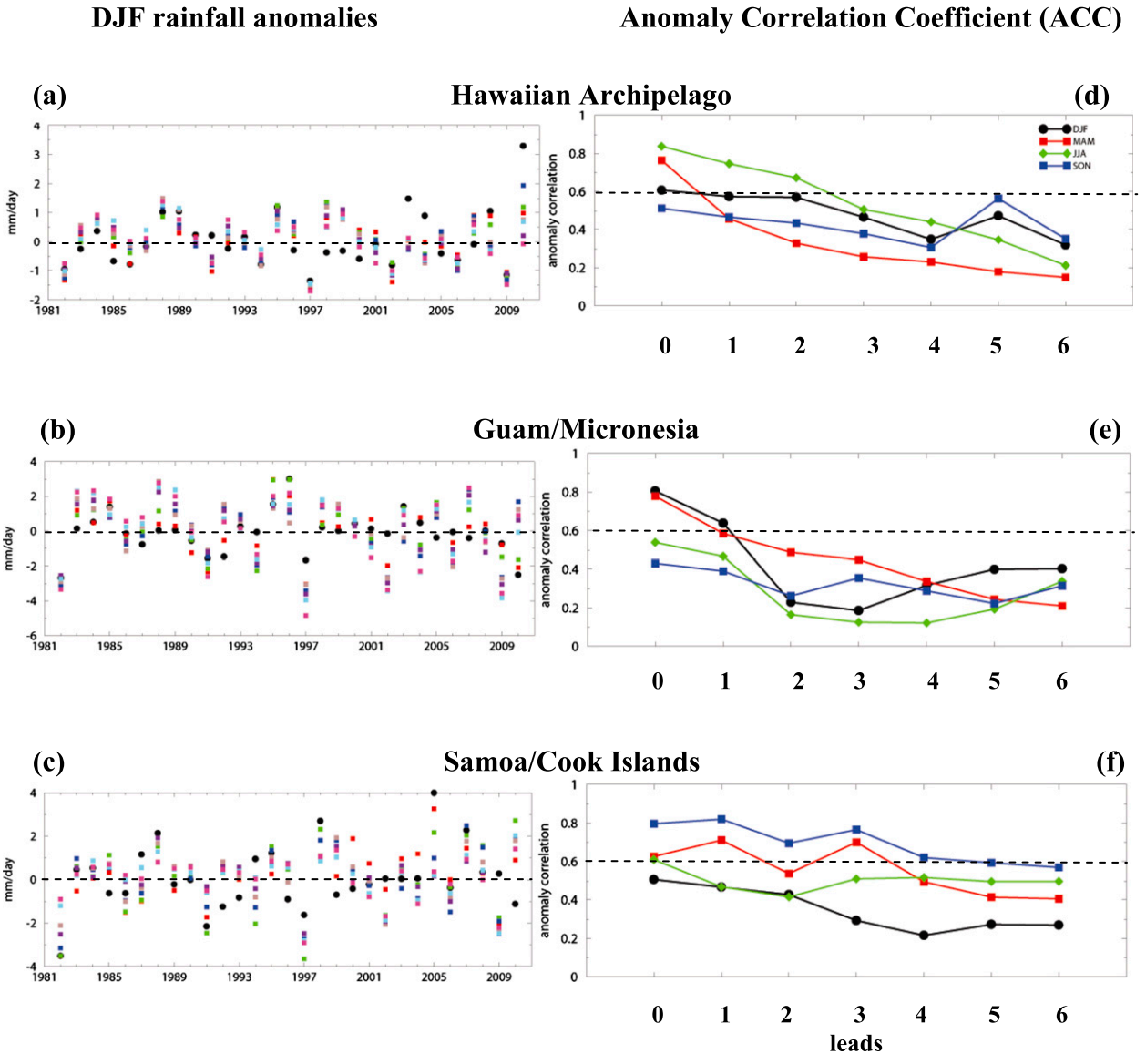

FIG. 11. Temporal evolution of CFSv2 hindcast at leads 0–6 months of winter (DJF) precipitation anomalies over (a) the Hawaiian Archipelago, (b) Guam and Micronesia, and (c) Samoa and the Cook Islands. The ACC for all seasons and at all leads for (d) the Hawaiian Archipelago, (e) Guam and Micronesia, and (f) Samoa and the Cook Islands. Dotted line in the right panels corresponds to ACC value of 0.6. Note that the symbols and colors for (a)–(c) are as in Fig. 6.

These individual terms for the winter of 1997/98 are displayed in Figs. 16 and 17. Tables 1–3 summarize contributions to $-\langle\omega\partial m/\partial p\rangle'$ from various forcing terms. A cautionary note is that a comparison with reanalysis does not guarantee CFSv2 results are correct since reanalysis is influenced by model biases in data-sparse regions. Next, we offer relevant interpretations that are common among Figs. 12–15.

For completeness, anomalous moisture convergence, precipitation, and low-level winds are also shown. Over the deep tropics, anomalous precipitation and moisture convergence share similar spatial patterns and strength (e.g., Figs. 12a,b), and the fact that convection and circulation are tightly coupled poses a severe constraint in attributing the cause and effect. Here, as in previous MSE-based model studies (Raymond 1995; Neelin and Su 2005), we treat convergence as a feedback to convection, and the various budget terms [Eq. (2)] as forcing for convection. In this context, gross moist stability (GMS)—the ratio between MSE export (Fig. 12c) and moisture convergence (Fig. 12b)—is positive with a value of 0.3–0.4 over regions of enhanced precipitation. The

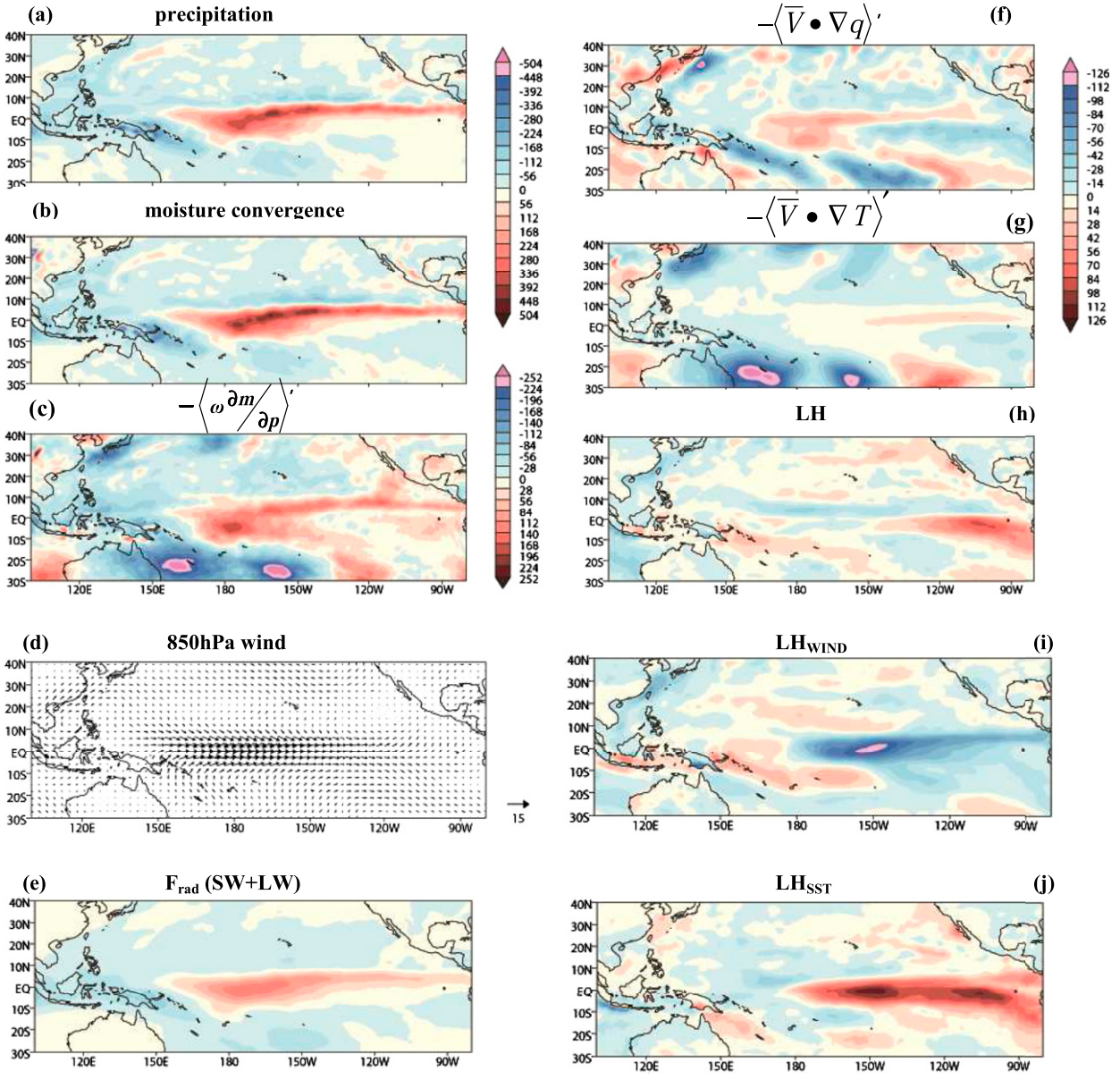

FIG. 12. Vertically integrated terms of the anomalous MSE budget computed from CFSv2 L0 hindcast for the fall season of the 1997/98 El Niño event: (a) precipitation, (b) moisture convergence, (c) MSE convergence $-\langle \omega \partial m/\partial p \rangle'$, (d) 850-hPa wind (m s^{-1}), (e) net radiative flux F_{rad}, (f) horizontal moisture advection $-\langle \overline{\mathbf{V}} \cdot \nabla q \rangle'$, (g) horizontal temperature advection $-\langle \overline{\mathbf{V}} \cdot \nabla T \rangle'$, (h) evaporation (LH), (i) evaporation attributable to wind (LH_{WIND}), and (j) evaporation attributable to SST (LH_{SST}). Except for 850-hPa wind, the units are watts per meter squared. Note that (a) and (b) share a common shading (interval of 56) and (e)–(j) share a different common shading (interval of 14). The ratio of MSE convergence to moisture convergence is considered GMS. The variables precipitation, moisture convergence, and 850-hPa wind anomalies are shown for easy interpretation.

GMS is a good measure of convective forcing and the resulting response of convection (Raymond et al. 2009). To infer GMS, moisture convergence is also shown in the figures.

MSE divergence regions (Fig. 12c) coincide with positive precipitation anomalies and represent thermally driven anomalous Hadley and Walker circulations. These divergent circulations are effective in transporting MSE, and air parcels moving poleward must have a higher MSE than air parcels moving equatorward (e.g., Fig. 14d). The positive (negative) values in $-\langle \overline{\mathbf{V}} \cdot \nabla q \rangle'$ reflect moist (dry) advection (Fig. 12f). In the deep tropics, contribution from $-\langle \overline{\mathbf{V}} \cdot \nabla T \rangle'$ is minimum owing to weak temperature gradient (Sobel and Bretherton 2000) but its

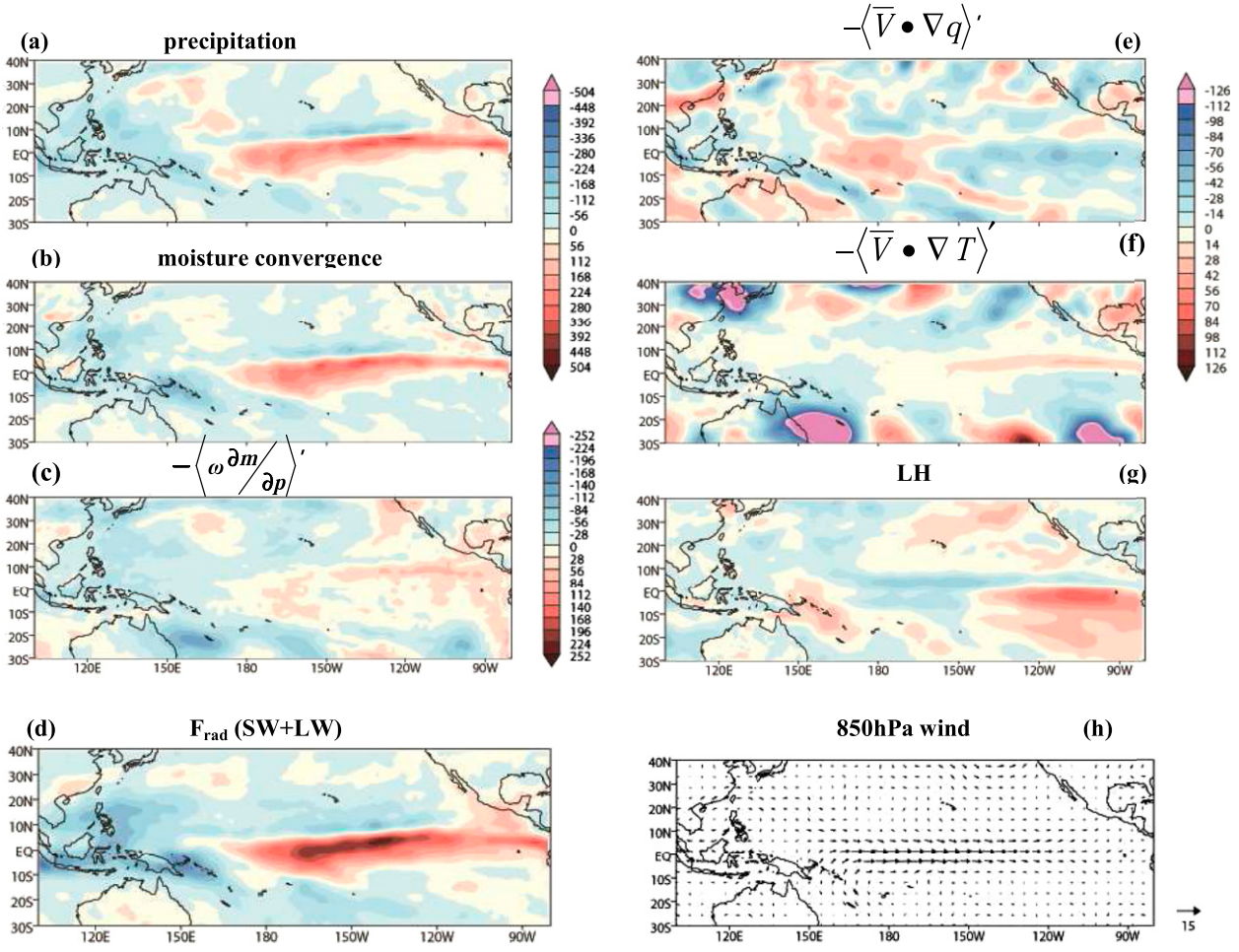

FIG. 13. Vertically integrated terms of the anomalous MSE budget computed from ERA-Interim reanalysis for the fall season of 1997/98 El Niño event: (a) precipitation (from GPCP), (b) moisture convergence, (c) MSE convergence $-\langle \omega \partial m/\partial p \rangle'$, (d) net radiative flux F_{rad}, (e) horizontal moisture advection $-\langle \overline{\mathbf{V}} \cdot \nabla q \rangle'$, (f) horizontal temperature advection $-\langle \overline{\mathbf{V}} \cdot \nabla T \rangle'$, (h) evaporation (LH), (h) 850 hPa wind ($m\,s^{-1}$). Except for 850 hPa wind, the units are watts per meter squared. Note that (a) and (b) share a common shading (interval of 56) and (d)–(g) share a common shading (interval of 14). The ratio of MSE convergence to moisture convergence is considered GMS. Variables precipitation, moisture convergence and 850 hPa wind anomalies are shown for easy interpretation.

wavy nature in the extratropics (Fig. 12g) represents barotropic Rossby waves forced by equatorial Pacific rainfall anomalies (Hoskins and Karoly 1981).

The anomalous net radiative flux (F_{rad}; Fig. 12e) accounts for cloud-radiative forcing, and therefore is proportional to rainfall anomalies. The interpretation is that cloudy regions are effective in trapping longwave radiation and thus experience reduction in radiative cooling. Subsequently, F_{rad} increases and acts as a feedback to convection. In contrast, regions of negative F_{rad} anomalies experience anomalous descent (adiabatic warming to balance radiative cooling). When F_{rad} is combined with MSE divergence (Fig. 12c), resultant spatial patterns look similar to moisture convergence.

Over the open oceans, $-\langle \overline{\mathbf{V}} \cdot \nabla q \rangle'$ and LH terms have opposite signatures (Figs. 12f,h), and low-level wind anomalies (Fig. 12d) aid in their interpretations. For CFSv2, partitioning of net evaporation anomalies (Fig. 12h) into that attributable to anomalous SST (Fig. 12j) and wind (Fig. 12i) shows opposing contributions. Identifying relative contributions between LH and $-\langle \overline{\mathbf{V}} \cdot \nabla q \rangle'$ in forcing rainfall anomalies is of interest here.

We will note that the leading mechanisms identified in CSFv2 are operational in reanalysis but the estimated MSE divergence is much weaker in the latter resulting in a weak GMS. On the other hand, the F_{rad} contribution to MSE budget is too strong in the reanalysis. Both in CFSv2 and the reanalysis the estimated budgets do not necessarily close. These issues are discussed in section 6. In the discussions to follow, general remarks mentioned above will not be repeated.

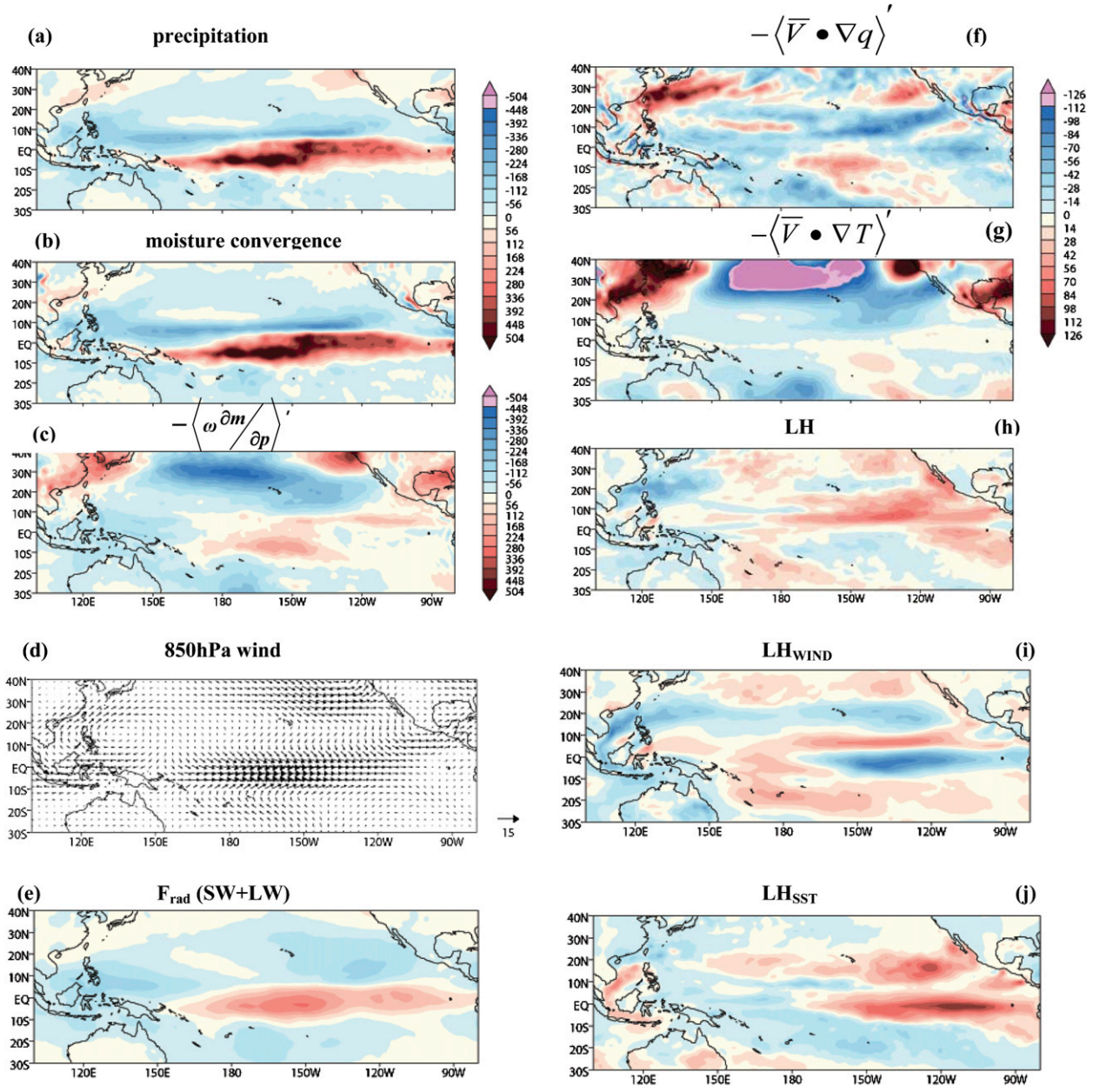

FIG. 14. As in Fig. 12, but for the winter season of the 1997/98 El Niño event.

a. MSE budget analysis during fall of 1997

1) BUDGET ANALYSIS ALONG THE EQUATORIAL PACIFIC

MSE divergence (Fig. 12c) is positive with a local maximum around the date line. In seeking balance, F_{rad} (39%) and moist advection (21%) prevail over negative evaporation anomalies (3%) along the equatorial central Pacific, while in the east (Table 1) evaporation increase (103%) and F_{rad} (55%) overcome dry advection (68%). The leading candidates and their contributions to the budget are noted in reanalysis too. Our conclusion is that moist advection and F_{rad} are leading mechanisms for convective anomalies around the date line whereas evaporation is most important in the east Pacific.

The effective roles of LH and $-\langle \overline{\mathbf{V}} \cdot \nabla q \rangle'$ can be understood as follows: low-level westerly anomalies (Fig. 12d) are effective in advecting climatological moisture from the equatorial western Pacific (Fig. 16c), and climatological easterlies (Fig. 4c) advect excess anomalous moisture from equatorial eastern Pacific (Fig. 16b), resulting in anomalous moist advection between 160°E and 160°W.

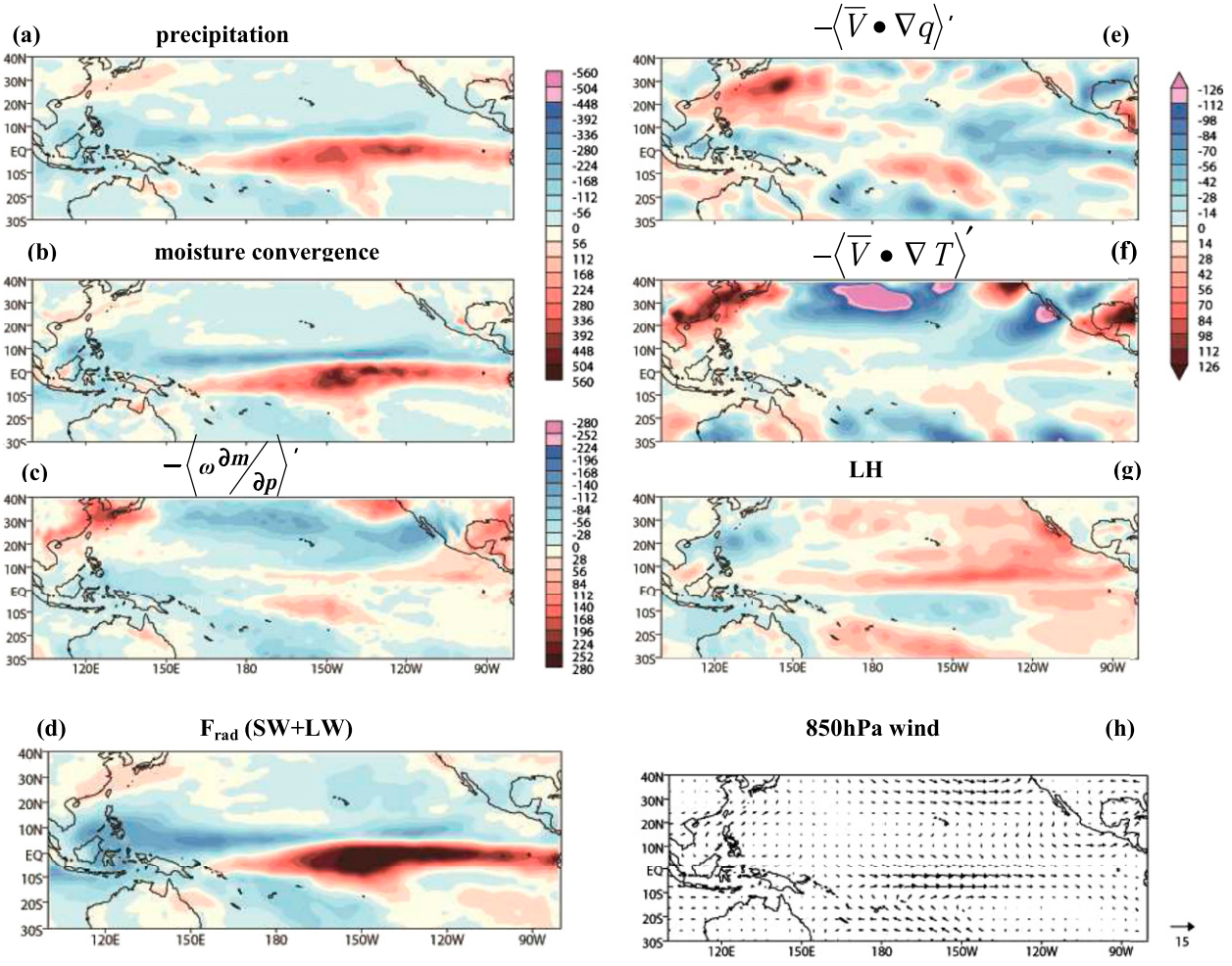

FIG. 15. As in Fig. 13, but for the winter season of the 1997/98 El Niño event.

Note that winter season results shown in Fig. 16 are also valid for the fall season (not shown). Simultaneously, anomalous westerlies flow against mean easterlies (Fig. 4), causing negative evaporation anomalies that maximize eastward of the date line (Fig. 12i). On the other hand, basinwide warm SST anomalies anchor positive evaporation anomalies over the central eastern Pacific (Fig. 12j). Therefore, net evaporation anomalies (Fig. 12h) are weakly negative around the date line but strongly positive between 140° and 80°W. Similar interpretations of LH and $-\langle \overline{\mathbf{V}} \cdot \nabla q \rangle'$ are valid for winter season too.

2) BUDGET ANALYSIS OVER THE USAPI

All the USAPI regions experience negative precipitation anomalies (Fig. 12a). Budget results are summarized in Table 2. Over the Hawaiian Islands, MSE divergence anomalies are balanced by advection of low MSE air from subtropics (65% from $-\langle \overline{\mathbf{V}} \cdot \nabla T \rangle'$ and 26% from $-\langle \overline{\mathbf{V}} \cdot \nabla q \rangle'$) and F_{rad} (32%). Over the archipelago, similar leading candidates account for drying. In both regions, contribution from LH cancels out with dry air advection. During fall, the descending arm of the anomalous local Hadley circulation is located poleward of the island chain, and the returning northerly anomalies (Fig. 12d) advect low MSE air, supporting the budget results.

For the negative rainfall anomalies over the Marshall Islands, reduced flux (LH, SH, and F_{rad}) contributions are partly offset by moist advection. Over Guam, the effect of F_{rad} (~22%) is reinforced by all the other terms (Table 2). Over the west Pacific, the presence of cold SST anomalies contributes to reduction of surface fluxes (e.g., Fig. 12j), and weak northerly anomalies at low-level advect low MSE, affecting Guam. Additionally, descending Rossby waves forced by central equatorial Pacific rainfall anomalies (Wang et al. 2000) amplify radiative cooling.

Over the South Pacific, a local maximum in MSE divergence anomalies is noted in each of the two regions (Fig. 12c). Over Fiji and the Melanesia region,

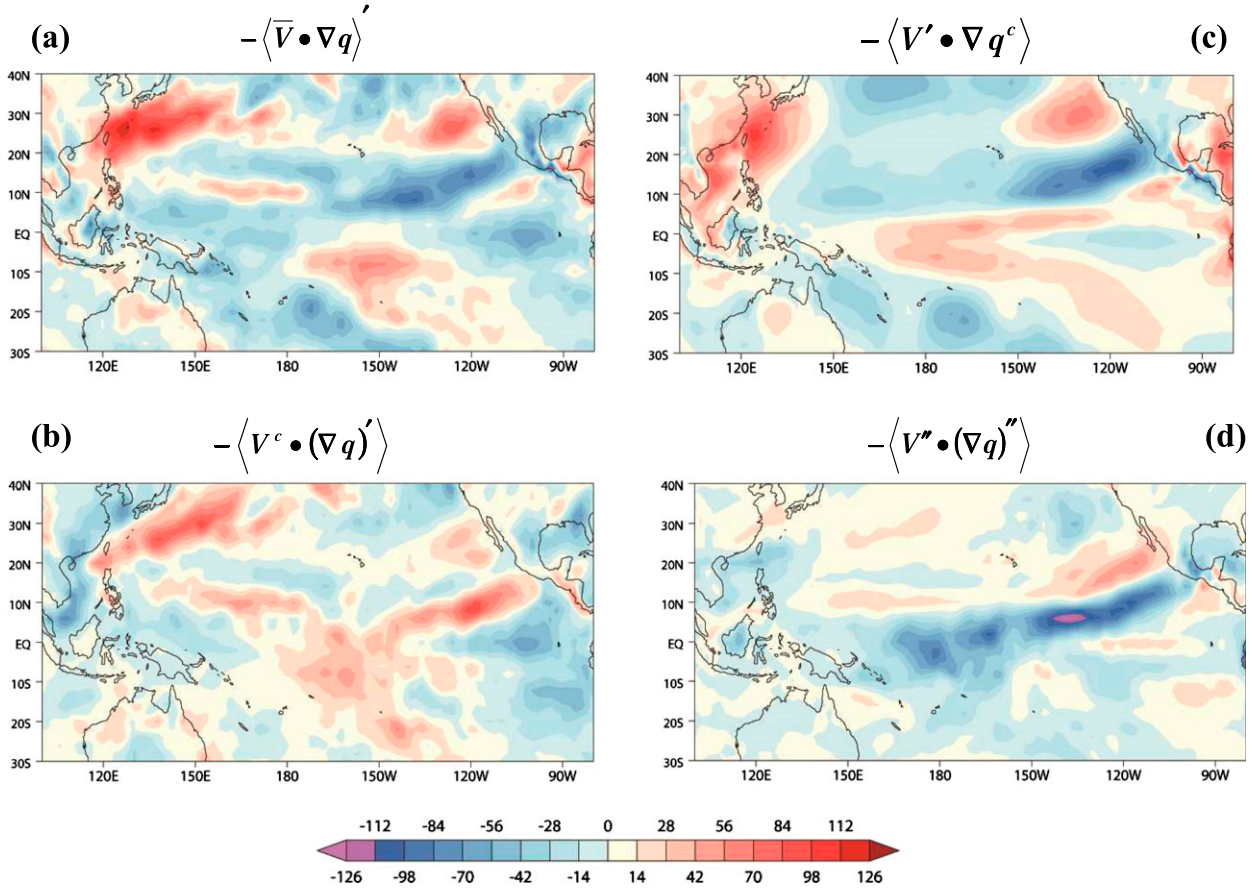

FIG. 16. Anomalous horizontal moisture advection ($W m^{-2}$) for winter of 1997/98 from CFSv2 hindcast: (a) total horizontal moisture advection $-\langle \overline{\mathbf{V}} \cdot \nabla q \rangle'$, (b) advection by climatological wind on anomalous moisture gradient $-\langle \mathbf{V}^c \cdot (\nabla q)' \rangle$, (c) advection by anomalous wind on climatological moisture gradient $-\langle \mathbf{V}' \cdot \nabla q^c \rangle$, and (d) advection by anomalous wind on anomalous moisture gradient $-\langle \mathbf{V}'' \cdot (\nabla q)'' \rangle$.

advection of low MSE air (49% from $-\langle \overline{\mathbf{V}} \cdot \nabla T \rangle'$ and 19% from $-\langle \overline{\mathbf{V}} \cdot \nabla q \rangle'$) and F_{rad} (10%) act in tandem, whereas LH (13%) opposes them. It is fair to say that these leading terms account for MSE divergence anomalies over Samoa and the Cook Islands too (Table 2). In the Southern Hemisphere, large-scale anomalous cyclonic circulation (Fig. 12d), a Rossby wave response to equatorial Pacific precipitation anomalies, is instrumental in advecting low MSE air from midlatitudes. Additionally, structures in $-\langle \overline{\mathbf{V}} \cdot \nabla T \rangle'$ imply signatures of barotropic Rossby waves forced by tropical heating anomalies. In the Southern Hemisphere, tropical–extratropical teleconnection is stronger during summer and fall (Trenberth et al. 1998).

For the drying conditions over USAPI, leading mechanisms identified in CFSv2 are in agreement with those of reanalysis (Fig. 13) but, quantitatively, contributions from F_{rad}, $-\langle \overline{\mathbf{V}} \cdot \nabla T \rangle'$, and LH are overly estimated in the reanalysis (Table 2).

b. MSE budget analysis during winter of 1997/98

During winter, basinwide positive rainfall anomalies between 10°S and 0° as well as negative rainfall anomalies over USAPI are much stronger (Fig. 14a) than during fall. As a consequence, MSE export is stronger (note the change in shading). Here, we focus on the leading candidates that account for the persistence and amplification of positive (negative) precipitation anomalies over the equatorial Pacific (USAPI). We note that relative contributions from various terms to the budget remain same with some deviations [Tables 1 (bottom) and 3]. We discuss mechanisms for the Pacific ITCZ drying and effects of the anomalous northerlies in the Northern Hemisphere tropics (Fig. 14d) on LH, $-\langle \overline{\mathbf{V}} \cdot \nabla T \rangle'$, and $-\langle \overline{\mathbf{V}} \cdot \nabla q \rangle'$. Finally, our results from CFSv2 and reanalysis are compared with those obtained from an intermediate model of Su and Neelin (2002).

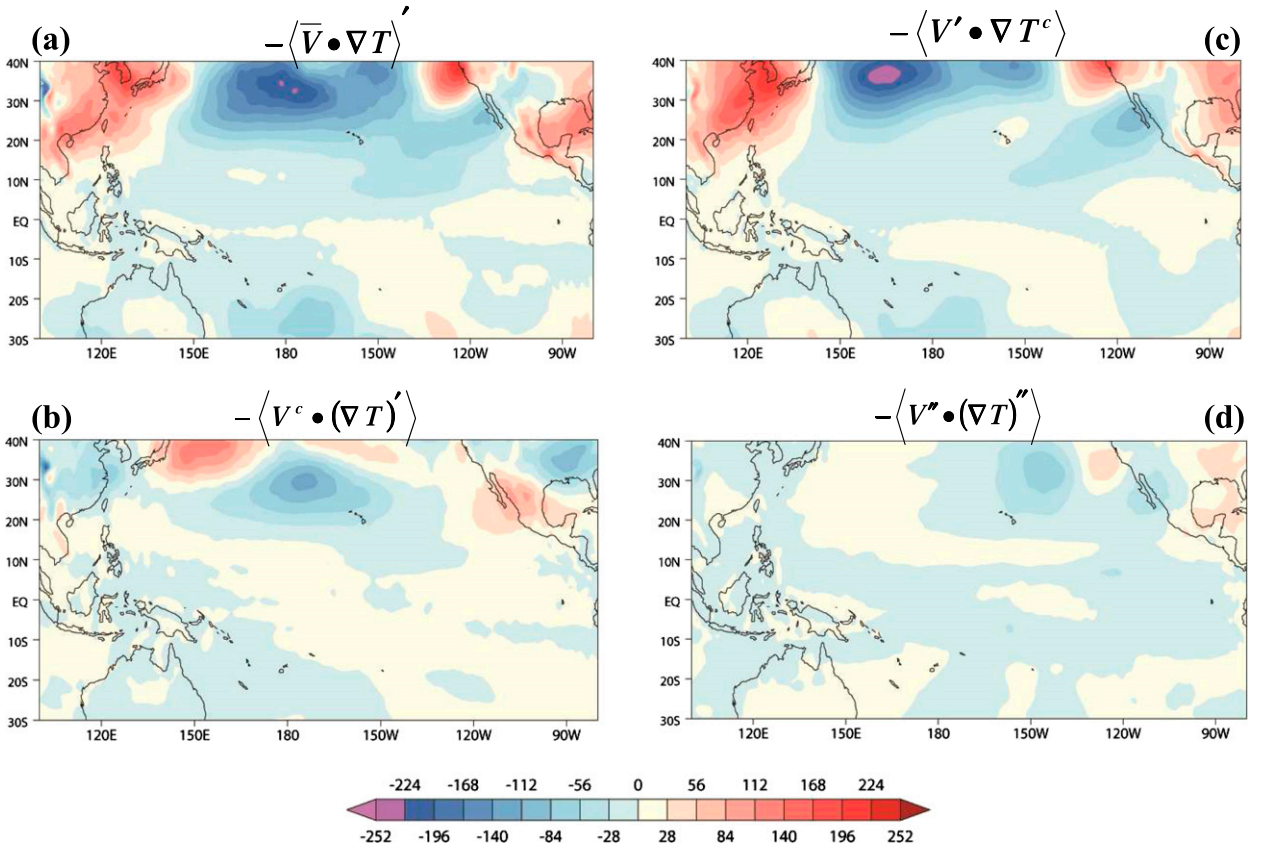

FIG. 17. Anomalous horizontal temperature advection ($W m^{-2}$) for winter of 1997/98 from CFSv2 hindcast: (a) total horizontal temperature advection $-\langle \overline{\mathbf{V}} \cdot \nabla T \rangle'$, (b) advection by climtaological wind on anomalous temperature gradient $-\langle \mathbf{V}^c \cdot (\nabla T)' \rangle$, (c) advection by anomalous wind on climtaological temperature gradient $-\langle \mathbf{V}' \cdot \nabla T^c \rangle$, and (d) advection by anomalous wind on anomalous temperature gradient $-\langle \overline{\mathbf{V}}'' \cdot (\nabla T)'' \rangle$.

1) BUDGET ANALYSIS ALONG THE EQUATORIAL PACIFIC

Over the equatorial central Pacific F_{rad}, $-\langle \overline{\mathbf{V}} \cdot \nabla q \rangle'$, and LH reinforce each other while along the eastern Pacific F_{rad} and LH, primarily because of SST anomalies (Fig. 14j), account for enhanced precipitation anomalies (Table 1). One deviation from fall (Fig. 12) lies in the contribution from anomalous LH over the central Pacific. Evaporation anomalies attributable to wind (Fig. 14i)

TABLE 1. MSE budget terms ($W m^{-2}$) area averaged over the central equatorial Pacific (10°S–5°N, 170°E–140°W) and eastern equatorial Pacific (5°S–5°N, 140°–80°W).

Season/model	$-\left\langle \omega \frac{\partial m}{\partial p} \right\rangle'$	$-\langle \overline{\mathbf{V}} \cdot \nabla q \rangle'$	$-\langle \overline{\mathbf{V}} \cdot \nabla T \rangle'$	LH′	SH′	$\langle \mathrm{LW} \rangle' + \langle \mathrm{SW} \rangle' = F'_{rad}$
			Central equatorial Pacific			
Fall 1997						
CFSv2	94 (100%)	20 (21%)	5 (6%)	−2 (−3%)	5 (5%)	37 (39%)
ERA-Interim	17 (100%)	15 (85%)	6 (34%)	−15 (−86%)	−2 (−12%)	56 (327%)
Winter 1997/98						
CFSv2	86 (100%)	17 (20%)	−1 (−1%)	10 (11%)	4 (4%)	40 (47%)
ERA-Interim	18 (100%)	13 (69%)	2 (13%)	4 (24%)	−3 (18%)	76 (414%)
			Eastern equatorial Pacific			
Fall 1997						
CFSv2	28 (100%)	−19 (−68%)	6 (21%)	29 (103%)	2 (7%)	15 (55%)
ERA-Interim	24 (100%)	−27 (−112%)	7 (28%)	30 (127%)	−1 (−4%)	49 (204%)
Winter 1997/98						
CFSv2	20 (100%)	−26 (−128%)	4 (21%)	23 (115%)	4 (19%)	30 (146%)
ERA-Interim	14 (100%)	−42 (−308%)	4 (26%)	25 (180%)	−3 (−20%)	80 (583%)

TABLE 2. MSE budget terms ($W\,m^{-2}$) area averaged over the Pacific islands during the fall 1997.

Region	Model	$-\left\langle \omega \frac{\partial m}{\partial p} \right\rangle'$	$-\langle \overline{\mathbf{V}} \cdot \nabla q \rangle'$	$-\langle \overline{\mathbf{V}} \cdot \nabla T \rangle'$	LH′	SH′	$\langle \mathrm{LW} \rangle' + \langle \mathrm{SW} \rangle' = F'_{\mathrm{rad}}$
Hawaii							
Main islands (18°–23°N, 160°–155°W)	CFSv2	−29 (100%)	−8 (26%)	−19 (65%)	7 (−25%)	1 (−2%)	−9 (32%)
	ERA-Interim	−24 (100%)	−2 (10%)	−28 (117%)	16 (−68%)	−3 (12%)	−10 (42%)
Archipelago (16°–28°N, 165°–150°W)	CFSv2	−35 (100%)	−7 (21%)	−22 (62%)	8 (−23%)	1 (−4%)	−6 (18%)
	ERA-Interim	−16 (100%)	−4 (22%)	−27 (168%)	15 (−95%)	−3 (17%)	−6 (39%)
West Pacific							
Marshall Islands (5°–10°N, 160°–180°E)	CFSv2	8 (100%)	7 (89%)	1 (13%)	−15 (−179%)	−2 (−27%)	−2 (−27%)
	ERA-Interim	−17 (100%)	7 (−40%)	2 (−14%)	−13 (76%)	3 (−17%)	13 (74%)
Guam (8°–15°N, 140°–160°E)	CFSv2	−38 (100%)	−4 (10%)	1 (−2%)	−5 (14%)	−1 (2%)	−8 (22%)
	ERA-Interim	−20 (100%)	3 (−13%)	4 (−17%)	−3 (17%)	1 (−4%)	−19 (92%)
South Pacific							
Samoa (25°–10°S, 160°–180°E)	CFSv2	−121 (100%)	−30 (25%)	−66 (55%)	13 (−11%)	2 (−2%)	−8 (6%)
	ERA-Interim	−43 (100%)	−7 (16%)	−42 (96%)	13 (−29%)	−1 (3%)	−12 (28%)
Melanesia (25°–10°S, 180°E–160°W)	CFSv2	−66 (100%)	−12(19%)	−32 (49%)	8 (−13%)	0 (0%)	−7(10%)
	ERA-Interim	−24 (100%)	0.8 (−2%)	−14 (60%)	8 (−32%)	0 (0%)	−12 (52%)

show that a narrow tongue of positive LH anomalies within approximately 5°–10°N, 160°E–100°W is sandwiched between bands of negative LH anomalies in either hemisphere. While the southern band is noted in fall (Fig. 12i), anomalous north-northwesterlies acting against climatological southeasterlies (Fig. 4d) result in the northern band of negative LH anomalies. The same anomalous winds act in concert with climatological winds to cause the narrow tongue of positive evaporation anomalies contributing to precipitation anomalies over central equatorial Pacific.

Negative precipitation anomalies along the Pacific ITCZ (5°–10°N) are largely attributable to advection of low MSE air (71% from $-\langle \overline{\mathbf{V}} \cdot \nabla q \rangle'$ and 27% from $-\langle \overline{\mathbf{V}} \cdot \nabla T \rangle'$), while LH (23%) opposes them. A breakdown of the moisture advection term (Fig. 16) shows that the anomalous northerlies east of 160°W (Fig. 14d) acting upon climatological (Fig. 16b) and anomalous moisture (Fig. 16d) gradients, as well as on climatological temperature gradients (Fig. 17b), account for the ITCZ drying. In summary, the stronger the equatorial Pacific positive precipitation anomalies are, the stronger is the local Hadley circulation whose return flow influence is felt as far as the Pacific ITCZ.

While budget estimates from reanalysis (Fig. 15) are broadly consistent with CFSv2 estimates, F_{rad} contributions overly dominate. The fact that F_{rad} is an outcome of cloud–radiation interactions leads us to wonder if these processes are faithfully represented.

2) BUDGET ANALYSIS OVER THE USAPI

Persistence of dryness over the USAPI regions is associated with MSE divergence anomalies with maximum amplitude noticeable over Hawaii, although negative precipitation anomalies are much stronger over the other regions. Over all the six regions, the leading mechanisms for drying and their share to the budget (Table 3) remain similar to those obtained in fall (Table 2). Over Hawaii, each term of the $-\langle \overline{\mathbf{V}} \cdot \nabla T \rangle'$ equation represents a local maximum (Fig. 17) and the interpretation is as follows. Over the North Pacific, climatological northwesterlies are prominent to the west of 160°W (Fig. 4d) and thus are efficient in the advection of anomalous cold air to the west (Fig. 17c), while the stronger anomalous northerlies to the east of 160°W are effective in advecting climatological (Fig. 17b) and anomalous (Fig. 17d) cold air to the east of the islands.

Over the South Pacific, negative precipitation and MSE divergence anomalies are stronger around Samoa and the Cook Islands than over Fiji and the Melanesia region. The leading agents for the persistence of drying over the South Pacific islands are advection of low MSE air (Table 3). Figures 16 and 17 indicate that $\langle \mathbf{V}' \cdot \nabla q^c \rangle$ and $\langle \mathbf{V}' \cdot \nabla T^c \rangle$ are the leading agents for the total anomalous dry and cold air advection, respectively.

Over the west Pacific islands, MSE divergence anomalies are very weak (Table 3). Over Guam and Micronesia, CFSv2 results suggest that contributions from moisture and temperature advections cancel out and F_{rad} maintains the dryness (Table 3). In contrast, reanalysis suggests that contributions from F_{rad} and LH anomalies are opposed by advection terms (Table 3). Similar disagreement is also noticeable over the Marshall Islands.

While our budget results broadly agree with those of Su and Neelin (2002), there are differences. In their

TABLE 3. MSE budget terms (W m^{-2}) area averaged over the Pacific islands during the winter of 1997/98.

Region	Model	$-\left\langle \omega \frac{\partial m}{\partial p} \right\rangle'$	$-\langle \overline{\mathbf{V}} \cdot \nabla q \rangle'$	$-\langle \overline{\mathbf{V}} \cdot \nabla T \rangle'$	LH′	SH′	$\langle \mathrm{LW} \rangle' + \langle \mathrm{SW} \rangle' = F'_{\mathrm{rad}}$
Hawaii							
Main islands (18°–23°N, 160°–155°W)	CFSv2	−193 (100%)	−2 (1%)	−59 (30%)	−11 (6%)	1 (0%)	−14 (7%)
	ERA-Interim	−54 (100%)	0 (0%)	−37 (69%)	9 (−17%)	−2 (4%)	−19 (36%)
Archipelago (16°–28°N, 165°–150°W)	CFSv2	−221 (100%)	−6 (3%)	−73 (33%)	−3 (1%)	1 (0%)	−15 (7%)
	ERA-Interim	−67 (100%)	−4 (6%)	−39 (59%)	14 (−21%)	−1 (2%)	−16 (24%)
West Pacific							
Marshall (5°–10°N, 160°–180°E)	CFSv2	4 (100%)	1 (37%)	−6 (−157%)	5 (141%)	−2 (−66%)	−11 (−282%)
	ERA-Interim	4 (100%)	15 (382%)	2 (63%)	12 (302%)	3 (87%)	−45 (−1129%)
Guam (8°–15°N, 140°–160°E)	CFSv2	−32 (100%)	5 (−17%)	−5 (16%)	1 (−2%)	−1 (2%)	−14 (45%)
	ERA-Interim	−4 (100%)	28 (−668%)	2 (−57%)	4 (105%)	2 (−38%)	−26 (618%)
South Pacific							
Samoa (25°–10°S, 160°–180°E)	CFSv2	−36 (100%)	−21 (58%)	−19 (53%)	24 (−66%)	0 (0%)	−5 (13%)
	ERA-Interim	−28 (100%)	−29 (104%)	−19 (70%)	22 (−80%)	0 (0%)	−19 (71%)
Melanesia (25°–10°S, 180°E–160°W)	CFSv2	−66 (100%)	−29 (44%)	−30 (46%)	10 (−15%)	−1 (1%)	−15 (22%)
	ERA-Interim	−37 (100%)	−14 (39%)	−28 (75%)	14 (−37%)	1 (−1%)	−21 (57%)

results, negative evaporation anomalies were identified as the leading factor for suppressed precipitation around the South Pacific islands. In CFSv2 hindcasts and reanalysis, we note positive evaporation anomalies there. This difference is because of anomalous circulation over 20°–5°S, 160°E–140°W, anticyclonic here (Fig. 14d), that acts in phase with the climatological flow (Fig. 4d) to enhance evaporation. Additionally, we recognize moist advection role in rainfall anomalies over the equatorial central Pacific.

6. Conclusions and discussion

a. Conclusions

Our goal is to develop a *framework*—one that has sound physical basis for dynamical seasonal prediction of precipitation over the insular Pacific islands. Toward that goal, we examined the ensemble hindcasts performed with CFSv2. We show that climates of the individual USAPI regions are dynamically linked to large-scale phenomena (Figs. 3 and 4). Regression analysis of precipitation, stratified on the Niño-3.4 index, suggests that ENSO is the leading predictability source for large and persisting precipitation anomalies over the USAPI (Figs. 7 and 8). We note that hindcasting El Niño–related SST and precipitation anomalies along the equatorial Pacific is skillful (Fig. 6). In terms of amplitude, forecast precipitation anomalies either along the equatorial Pacific (Fig. 6) or over the USAPI regions (Figs. 10 and 11) approach observations as lead time approaches 0 months. Compared to its earlier version reported in Sooraj et al. (2012), CFSv2 skill in predicting USAPI regional precipitation anomalies shows improvement (Fig. 9).

Our framework expects that prediction skill is for physically correct reasons. Our hypothesis is, essentially, that skill underscores the realistic representation of moist and radiative processes in CFSv2. To test this hypothesis, we applied MSE budget analysis (Figs. 12–17). In both CFSv2 and reanalysis, different terms determine positive precipitation anomalies along different sectors of the equatorial Pacific during El Niño. Specifically, moist advection, attributable to anomalous wind acting on the climatological moisture gradient, contributes to positive precipitation anomalies around the date line, whereas enhanced evaporation, attributable to warmer SST anomalies, induces precipitation anomalies along the eastern equatorial Pacific. In both regions, net radiative flux anomalies provide feedback. Over the South Pacific and Hawaiian Islands, circulation anomalies forced by equatorial Pacific precipitation anomalies advect subtropical dry and cold air southward, causing persistent dryness. Over the west Pacific islands, surface and net radiative fluxes determine precipitation anomalies. Our conclusion is that all the terms in MSE budget are important in forcing convection along the equatorial Pacific, as well as over the USAPI, during the life cycle of the 1997/98 El Niño, and in other ENSO years (not shown). We conclude that the CFSv2 budget estimates qualitatively agree with those estimated from reanalysis. The limitations in the budget diagnostics and way forward are discussed below.

Notwithstanding the overall success of CFSv2, ACC values in different seasons suggest low skill over Hawaii and the west Pacific during their rainy seasons (Fig. 11). Of the regions examined here, CFSv2 shows highest skill over the southwest Pacific islands. Because of its observed low seasonal mean precipitation and variance (Figs. 2 and 5), forecast skill over Hawaii remains low. During the monsoon season, low skill over the west Pacific islands may be attributed to internal variability associated with intraseasonal oscillations (Sperber and Annamalai 2008) or mutual influences among the regional heat sources (Annamalai and Sperber 2005) and local air–sea interactions (Wang et al. 2000). Future research is necessary to better understand seasonal dependency in skill. As suggested by Alessandri et al. (2011), seasonal prediction skill over land is about half of the skill over the ocean. Here, both land and ocean grid points are considered in the area average that is expected to inflate the skill over the USAPI. Our future efforts will address this issue.

b. Discussion

We recognize that one major stumbling block for the implementation of our framework is the large budget residuals (Table 3), implying misrepresentation of certain moist and radiative processes. Additionally, weak (strong) amplitude in MSE divergence (net radiative flux) anomalies in reanalysis limits a "true" validation with model results. We discuss various sources for budget residuals and future directions.

Estimated MSE divergence $-\langle\omega\partial m/\partial p\rangle'$ depends on the model's ability in accurately representing vertical velocity, which in turn depends on the cumulus parameterization employed (Raymond et al. 2009). In CFSv2 and reanalysis, an examination of equatorial central-eastern Pacific area-averaged anomalous ω during winter of 1997/98 El Niño (not shown) indicates consistency in the vertical structure; however, amplitude in the reanalysis is about 50% weaker than in CFSv2. Additionally, an evaluation of the vertical profile in $-\langle\omega\partial m/\partial p\rangle'$ shows good agreement for the low-level peak, but the reanalysis misses the midlevel peak (not shown). We note that computation of MSE from reanalysis has substantial errors and uncertainties (Black and Bretherton 2006; Prasanna and Annamalai 2012) because vertical velocity is not observed, but rather is inferred from a data assimilation process. Furthermore, moisture convergence closure is incorporated in the Tiedtke (1989) convective parameterization scheme employed in ERA-Interim, a factor that can underestimate $-\langle\omega\partial m/\partial p\rangle'$. Clearly, further direct observations are needed to verify if the Arakawa–Schubert scheme employed in CFSv2 captures realistic vertical velocity profiles.

Both reanalysis and CFSv2 budgets suggest that in regions of enhanced (suppressed) precipitation the cloud–radiative term $F_{\rm rad}$ is positive (negative). This term is coupled with the large-scale circulation through its effect on diabatic heating, which affects both the amount and type of cloud (Hartmann et al. 2001). Considering that radiative processes are not observed, but depend instead on model physics employed in the reanalysis system, and recognizing its "super active" role in the reanalysis budget, investigation of the vertical cloud structure is warranted both in CFSv2 and reanalysis products. We note that the $F_{\rm rad}$ contribution to $-\langle\omega\partial m/\partial p\rangle'$ identified in CFSv2 is comparable to that of the intermediate model results of Su and Neelin (2002).

It should be mentioned that that MSE divergence arises from cancellation between large terms in temperature (diabatic heating) and moisture (convergence of moisture) tendency equations. Therefore, the MSE budget is sensitive to interpolation particularly in climate models that employ terrain-following sigma coordinates while standard output is interpolated to pressure levels. Additionally, advection schemes employed here differ from the ones used in the original model codes. In an ongoing effort, budget terms are preserved in model grids and the results will be reported soon.

Given the dearth of direct field observations, identifying possible source of errors explaining the inconsistency between CFSv2 and reanalysis estimates of $-\langle\omega\partial m/\partial p\rangle'$ and $F_{\rm rad}$ is difficult. A way forward, perhaps, is to have sustained direct observations of three-dimensional moisture and radiative fields over the tropics. Such an observational effort would constrain and improve model parameterizations, although direct observations over the open oceans have practical limitations. Perhaps an immediate way forward is to assess a suite of coupled model hindcasts, such as those performed under the U.S. National Multi-Model Ensemble auspices (Kirtman et al. 2014), and validate MSE budgets of each model against available reanalysis products. We hope that convergence of robustness among the different models may lean toward "truth."

Acknowledgments. This study is supported by the NOAA Climate Test Bed (CTB) program and also partly funded by the institutional grants of the IPRC. CFSv2 hindcasts for budget estimates were provided by the National Climatic Data Center. Dr. Mat Widlansky is thanked for comments and proofreading. Comments from anonymous reviewers are acknowledged.

REFERENCES

Alessandri, A., A. Borrelli, A. Navarra, A. Arribas, M. Déqué, P. Rogel, and A. Weisheimer, 2011: Evaluation of probabilistic

quality and value of the ENSEMBLES multi-model seasonal forecasts: Comparison with DEMETER. *Mon. Wea. Rev.,* **139,** 581–607, doi:10.1175/2010MWR3417.1.

Annamalai, H., 2010: Moist dynamical linkage between the equatorial Indian Ocean and the South Asian monsoon trough. *J. Atmos. Sci.,* **67,** 589–610, doi:10.1175/2009JAS2991.1.

——, and P. Liu, 2005: Response of the Asian summer monsoon to changes in ENSO properties. *Quart. J. Roy. Meteor. Soc.,* **131,** 805–831, doi:10.1256/qj.04.08.

——, and K. R. Sperber, 2005: Regional heat sources and the active and break phases of the boreal summer intraseasonal (30–50 day) variability. *J. Atmos. Sci.,* **62,** 2726–2748, doi:10.1175/JAS3504.1.

——, P. Liu, and S.-P. Xie, 2005: Southwest Indian Ocean SST variability: Its local effect and remote influence on Asian monsoons. *J. Climate,* **18,** 4150–4167, doi:10.1175/JCLI3533.1.

——, H. Okajima, and M. Watanabe, 2007: Possible impact of the Indian Ocean SST on the Northern Hemisphere circulation during El Niño. *J. Climate,* **20,** 3164–3189, doi:10.1175/JCLI4156.1.

Arakawa, A., and W. H. Schubert, 1974: Interaction of a cumulus cloud ensemble with the large-scale environment. Part I. *J. Atmos. Sci.,* **31,** 674–701, doi:10.1175/1520-0469(1974)031<0674:IOACCE>2.0.CO;2.

Berrisford, P., D. Dee, K. Fielding, M. Fuentes, P. Kallberg, S. Kobayashi, and S. Uppala, 2009: The ERA-Interim archive. ERA Rep. Series, Vol. 1, 16 pp.

Black, L. E., and C. S. Bretherton, 2006: Geographic variability in the export of moist static energy and vertical motion profiles in the tropical Pacific. *Geophys. Res. Lett.,* **33,** L17810, doi:10.1029/2006GL026672.

Caplan, P., J. Derber, W. Gemmill, S.-Y. Hong, H.-L. Pan, and D. Parrish, 1997: Changes to the 1995 NCEP operational medium-range forecast model analysis–forecast system. *Wea. Forecasting,* **12,** 581–594, doi:10.1175/1520-0434(1997)012<0581:CTTNOM>2.0.CO;2.

Chen, P., M. P. Hoerling, and R. M. Dole, 2001: The origin of the subtropical anticyclone. *J. Atmos. Sci.,* **58,** 1827–1835, doi:10.1175/1520-0469(2001)058<1827:TOOTSA>2.0.CO;2.

Cottrill, A., and Coauthors, 2013: Seasonal forecasting in the Pacific using the coupled model POAMA-2. *Wea. Forecasting,* **28,** 668–680, doi:10.1175/WAF-D-12-00072.1.

Hartmann, D. L., L. A. Moy, and Q. Fu, 2001: Tropical convection and the energy balance at the top of the atmosphere. *J. Climate,* **14,** 4495–4511, doi:10.1175/1520-0442(2001)014<4495:TCATEB>2.0.CO;2.

Hoskins, B. J., and D. J. Karoly, 1981: The steady linear response of a spherical atmosphere to thermal and orographic forcing. *J. Atmos. Sci.,* **38,** 1179–1196, doi:10.1175/1520-0469(1981)038<1179:TSLROA>2.0.CO;2.

Huffman, G. J., and Coauthors, 2007: The TRMM Multisatellite Precipitation Analysis: Quasi-global, multiyear, combined-sensor precipitation estimates at fine scale. *J. Hydrometeor.,* **8,** 38–55, doi:10.1175/JHM560.1.

——, R. F. Adler, D. T. Bolvin, and G. Gu, 2009: Improving the global precipitation record: GPCP version 2.1. *Geophys. Res. Lett.,* **36,** L17808, doi:10.1029/2009GL040000.

Janicot, S., A. Harzallah, B. Fontaine, and V. Moron, 1998: West African monsoon dynamics and eastern equatorial Atlantic and Pacific SST anomalies (1970–88). *J. Climate,* **11,** 1874–1882, doi:10.1175/1520-0442-11.8.1874.

Kirtman, B., and A. Pirani, 2009: The state of the art of seasonal prediction: Outcomes and recommendations from the First World Climate Research Program Workshop on Seasonal Prediction. *Bull. Amer. Meteor. Soc.,* **90,** 455–458, doi:10.1175/2008BAMS2707.1.

——, and Coauthors, 2014: The North American Multi-Model Ensemble (NMME): Phase 1, Seasonal to interannual prediction, and phase 2, toward developing intra-seasonal prediction. *Bull. Amer. Meteor. Soc.,* in press.

Kumar, A., and M. Hoerling, 1998: Annual cycle of Pacific–North American predictability associated with different phases of ENSO. *J. Climate,* **11,** 3295–3308, doi:10.1175/1520-0442(1998)011<3295:ACOPNA>2.0.CO;2.

——, M. Chen, L. Zhang, W. Wang, Y. Xue, C. Wen, L. Marx, and B. Huang, 2012: An analysis of the nonstationarity in the bias of sea surface temperature forecasts for the NCEP Climate Forecast System (CFS) version 2. *Mon. Wea. Rev.,* **140,** 3003–3016, doi:10.1175/MWR-D-11-00335.1.

Nagamura, H., and T. Miyasaka, 2004: Formation of summertime subtropical highs. *Bull. Amer. Meteor. Soc.,* **85,** 1062–1064.

Neelin, J. D., and I. M. Held, 1987: Modeling tropical convergence based on the moist static energy budget. *Mon. Wea. Rev.,* **115,** 3–12, doi:10.1175/1520-0493(1987)115<0003:MTCBOT>2.0.CO;2.

——, and H. Su, 2005: Moist teleconnection mechanisms for the tropical South American and Atlantic sector. *J. Climate,* **18,** 3928–3950, doi:10.1175/JCLI3517.1.

Peng, P., A. Kumar, and W. Wang, 2011: An analysis of seasonal predictability in coupled model forecasts. *Climate Dyn.,* **36,** 637–648, doi:10.1007/s00382-009-0711-8.

Prasanna, V., and H. Annamalai, 2012: Moist dynamics of extended monsoon breaks over South Asia. *J. Climate,* **25,** 3810–3831, doi:10.1175/JCLI-D-11-00459.1.

Raymond, D. J., 1995: Regulation of moist convection over the West Pacific warm pool. *J. Atmos. Sci.,* **52,** 3945–3959, doi:10.1175/1520-0469(1995)052<3945:ROMCOT>2.0.CO;2.

——, S. L. Sessions, A. H. Sobel, and Z. Fuchs, 2009: The mechanics of gross moist stability. *J. Adv. Model. Earth Syst.,* **1** (9), doi:10.3894/JAMES.2009.1.9.

Reynolds, R. W., N. A. Raynor, T. M. Smith, D. C. Stokes, and W. Wang, 2002: An improved in situ and satellite SST analysis for climate. *J. Climate,* **15,** 1609–1625, doi:10.1175/1520-0442(2002)015<1609:AIISAS>2.0.CO;2.

Rodwell, M. J., and B. J. Hoskins, 2001: Subtropical anticyclones and summer monsoons. *J. Climate,* **14,** 3192–3211, doi:10.1175/1520-0442(2001)014<3192:SAASM>2.0.CO;2.

Ropelewski, C. F., and M. S. Halpert, 1987: Global and regional scale precipitation associated with El Niño/Southern Oscillation. *Mon. Wea. Rev.,* **115,** 1606–1626, doi:10.1175/1520-0493(1987)115<1606:GARSPP>2.0.CO;2.

Saha, S., and Coauthors, 2010: The NCEP Climate Forecast System Reanalysis. *Bull. Amer. Meteor. Soc.,* **91,** 1015–1057, doi:10.1175/2010BAMS3001.1.

——, and Coauthors, 2014: The NCEP Climate Forecast System version 2. *J. Climate,* **27,** 2185–2208, doi:10.1175/JCLI-D-12-00823.1.

Seager, R., R. Murtugudde, N. Naik, A. Clement, N. Gordon, and J. Miller, 2003: Air–sea interaction and the seasonal cycle of the subtropical anticyclone. *J. Climate,* **16,** 1948–1966, doi:10.1175/1520-0442(2003)016<1948:AIATSC>2.0.CO;2.

Shukla, J., 1998: Predictability in the midst of chaos: A scientific basis for climate forecasting. *Science,* **282,** 728–731, doi:10.1126/science.282.5389.728.

Sobel, A. H., and C. S. Bretherton, 2000: Modeling tropical precipitation in a single column. *J. Climate,* **13,** 4378–4392, doi:10.1175/1520-0442(2000)013<4378:MTPIAS>2.0.CO;2.

Sooraj, K. P., H. Annamalai, A. Kumar, and H. Wang, 2012: A comprehensive assessment of CFS seasonal forecasts over the tropics. *Wea. Forecasting,* **27,** 3–27, doi:10.1175/WAF-D-11-00014.1.

Sperber, K. R., and H. Annamalai, 2008: Coupled model simulations of boreal summer intraseasonal (30–50 day) variability, Part I: Systematic errors and caution on use of metrics. *Climate Dyn.,* **31,** 345–372, doi:10.1007/s00382-008-0367-9.

——, J. M. Slingo, and H. Annamalai, 2000: Predictability and the relationship between subseasonal and interannual variability during the Asian summer monsoon. *Quart. J. Roy. Meteor. Soc.,* **126,** 2545–2574, doi:10.1002/qj.49712656810.

Su, H., and J. D. Neelin, 2002: Teleconnection mechanism for tropical Pacific descent anomalies during El Niño. *J. Atmos. Sci.,* **59,** 2694–2712, doi:10.1175/1520-0469(2002)059<2694:TMFTPD>2.0.CO;2.

——, ——, and C. Chou, 2001: Tropical teleconnection and local response to SST anomalies during the 1997–1998 El Nino. *J. Geophys. Res.,* **106** (D17), 20 025–20 043, doi:10.1029/2000JD000124.

Tiedtke, M., 1989: A comprehensive mass flux scheme for cumulus parameterization in large-scale models. *Mon. Wea. Rev.,* **117,** 1779–1800, doi:10.1175/1520-0493(1989)117<1779:ACMFSF>2.0.CO;2.

Trenberth, K. E., 1976: Spatial and temporal variations of the Southern Oscillation. *Quart. J. Roy. Meteor. Soc.,* **102,** 639–653, doi:10.1002/qj.49710243310.

——, G. W. Branstator, D. Karoly, A. Kumar, N-C. Lau, and C. Ropelewski, 1998: Progress during TOGA in understanding and modeling global teleconnections associated with tropical sea surface temperatures. *J. Geophys. Res.,* **103,** 14 291–14 324, doi:10.1029/97JC01444.

Vincent, D. G., 1994: The South Pacific convergence zone (SPCZ): A review. *Mon. Wea. Rev.,* **122,** 1949–1970, doi:10.1175/1520-0493(1994)122<1949:TSPCZA>2.0.CO;2.

Vincent, E. M., M. Lengaigne, C. E. Menkes, N. C. Jourdain, P. Marchesiello, and G. Madec, 2011: Interannual variability of the South Pacific convergence zone and implications for tropical cyclone genesis. *Climate Dyn.,* **36,** 1881–1896, doi:10.1007/s00382-009-0716-3.

Wallace, J. M., and D. S. Gutzler, 1981: Teleconnections in the potential height field during the Northern Hemisphere winter. *Mon. Wea. Rev.,* **109,** 784–812, doi:10.1175/1520-0493(1981)109<0784:TITGHF>2.0.CO;2.

Wang, B., R. Wu, and X. Fu, 2000: Pacific–East Asia teleconnection: How does ENSO affect East Asian climate? *J. Climate,* **13,** 1517–1536, doi:10.1175/1520-0442(2000)013<1517:PEATHD>2.0.CO;2.

Widlansky, M. J., P. J. Webster, and C. D. Hoyos, 2011: On the location and orientation of the South Pacific convergence zone. *Climate Dyn.,* **36,** 561–578, doi:10.1007/s00382-010-0871-6.

Xue, Y., B. Huang, Z.-Z. Hu, A. Kumar, C. Wen, D. Behringer, and S. Nadiga, 2011: An assessment of oceanic variability in the NCEP Climate Forecast System Reanalysis. *Climate Dyn.,* **37,** 2511–2539, doi:10.1007/s00382-010-0954-4.

——, M. Chen, A. Kumar, Z.-Z. Hu, and W. Wang, 2013: Prediction skill and bias of tropical Pacific sea surface temperatures in the NCEP Climate Forecast System version 2. *J. Climate,* **26,** 5358–5378, doi:10.1175/JCLI-D-12-00600.1.